1-1-2016

Numerical Investigation of Airfoil Self-Noise Generation at Low Reynolds Number

Tarik Lyas

Numerical investigation of airfoil self-noise generation at low Reynolds number

By

Tarik Lyas

A Thesis
Submitted to the Faculty of
Mississippi State University
in Partial Fulfillment of the Requirements
for the Degree of Master of Science
in Aerospace Engineering
in the Department of Aerospace Engineering

Mississippi State, Mississippi

December 2016

Numerical investigation of airfoil self-noise generation at low Reynolds number

By

Tarik Lyas

Approved:

_____

Adrian Sescu
(Major Professor)

_____

J. Mark Janus
(Graduate Coordinator/Committee Member)

_____

Pasquale Cinnella
(Committee Member)

_____

Jason keith
Dean
Bagley College of Engineering

Name:Tarik Lyas

Date of Degree: December 9, 2016

Institution: Mississippi State University

Major Field: Aerospace Engineering

Major Professor: Adrian Sescu

Title of Study: Numerical investigation of airfoil self-noise generation at low Reynolds number

Pages in Study75

Candidate for Degree of Master of Science

In the advent of increasing the number of operable unmanned aerial systems (UAS) over the next years, a challenge exists in regard to the noise signature that these machines may generate. In this work, we perform advanced computational simulations to study the flow around an airfoil and the associated noise radiating to the near- and far-field. The airfoil size and the freestream velocity are representative of a typical UAS.

The study is aimed at investigating the characteristics of the aerodynamic noise radiating from an airfoil at various angles of attack, Reynolds number and Mach number. The numerical tool is a high-order compressible Navier-Stokes solver, using Runge-Kutta explicit time integration and dispersion-relation-preserving spatial discretization. Various results in terms of velocity and pressure distribution around the airfoil, and sound pressure level spectra calculated from different probe points located in the near- and far-field are compared to each other and discussed.

ACKNOWLEDGEMENTS

I would like to express my gratitude to Dr. Adrian Sescu, Assistant Professor in the Aerospace Engineering department, Mississippi State University, who has advised me accomplish this thesis since the beginning of my graduate studies. I am grateful for his guidance, support, and intellectual advice that helped me develop my research skill and autonomy. The present work would not have been possible without his patient and his time.

I also wish to express my appreciation to Mississippi state university for this big opportunity, it has helped me extend my knowledge and meet interesting people whom helped me throughout all this unforgivable experience.

I would also like to show my appreciation to John Haywood and Bill Sassanis for helping me in my research and the present paper, without them this work would not be possible in this short amount of time.

I am grateful to my fellow classmates who kept me company and supported me during the countless hours of experiments.

Last but not least, I wouldn't be studying at Mississippi State University if it was not for my parents, without them I couldn't experience such an opportunity. I would like to dedicate this work to my parents for their tremendous help throughout all this years, at all times.

TABLE OF CONTENTS

APPENDIX

LIST OF TABLES

LIST OF FIGURES

CHAPTER I

INTRODUCTION

The prediction of aerodynamic noise is a challenging phenomenon in the aeroacoustics community. It is mostly caused by jet exhaust, fan, power-plant, turbo-machinery, etc.

One particular area is the noise generated by the interaction of the boundary layer and the wake generated by an airfoil. The study included in this thesis is motivated by the growing number of unmanned aerial systems that are produced today. In particular, the noise generated by these machines may be annoying to people that live nearby the flight paths of UAS. Although most of the noise generated by a typical UAS is coming from the propeller or the motor, there are other sources that may contribute to the overall noise.

The present study is the cumulative result of advanced computational simulations targeted to study the behavior of the flow around an airfoil at various angle of attack.

A classical trailing-edge noise theory was proposed by Amiet [1]. It has proven to be an efficient approach because the far field noise can be precisely predicted as long as the surface pressure differs. According to Brooks [2], the four mechanisms responsible for airfoil self-noise are produced largely by the interaction of disturbances with the airfoil trailing edge. In addition, Brooks states that there is a fifth important mechanism, represented by the noise from wing-tip vortex. However, some additional noise sources beside the airfoil trailing edge have been observed recently.

1.1 Aircraft noise

The civil aviation is forecasted to grow over the next 30 years at an average rate of 4.25% [3]. These forecasts are likely to meet all the airlines capacity demands according to the Department of Transportation. In addition, the world trade value and the economic activities have contributed to the increase of the global economy. Also, the number of air travelers is doubled every 15-20 years.

The noise the aircraft generate continues to have a challenging impact on the aviation, as well as on the health of human beings. Studies have reported complaints of many residents living around airports; these complaints include severe health issues such as annoyance, sleep disturbance, and other effects.

According to the Government, noise can be "one of the most objectionable impacts of airport development." [4]. Aircraft noise can affect tremendously the quality of life of people living around the airports, and it can lead to anger, frustrations, lack of concentration, and sleeplessness. Many findings that were published in this area are either contradictory or inconclusive.

1.2 Background

The noise radiated from an aircraft is quite complex, and is commonly heard from the jet exhaust, fan, power-plant, turbo-machinery, etc(the important noise sources are depicted in Fig 1.1). It can be classified into propulsive noise and airframe noise. The propulsive noise is the noise heard from the engine fan and jet, while the airframe noise is produced by all other aircraft structures.

Aircraft noise can be split in four categories: jet noise that occurs when the exhaust's high velocity is mixed with the ambient air, combustor noise which is

associated with the rapid oxidation of jet fuel and the associated release of energy, turbomachinery noise is perceived when the distance between the source and the aircraft is small, and aerodynamic noise which is associated with rapid air movement over the airframe and control surfaces. The aerodynamic noise still remains as a major noise that challenges the future aviation, whereas both combustor and turbomachinery noise are significantly decreased due to the technological improvement in the new aircrafts.

The most important noise sources vary between take-off and landing. Fig 1.2 shows that the major contribution comes from the jet noise and fan noise during the take-off and that the fan noise is the dominant noise source from the engine during approach, followed by airframe noise radiated from the landing gear and flaps/slats [5].

The interaction of incoming flow airflow with the leading edge of the blades is what causes the fan noise. It creates trailing edge noise, known as airfoil self-noise which is the main topic of investigation in investigation in this thesis.

Figure 1.1 Major noise sources of the airframe and engine of a civil aircraft [5]

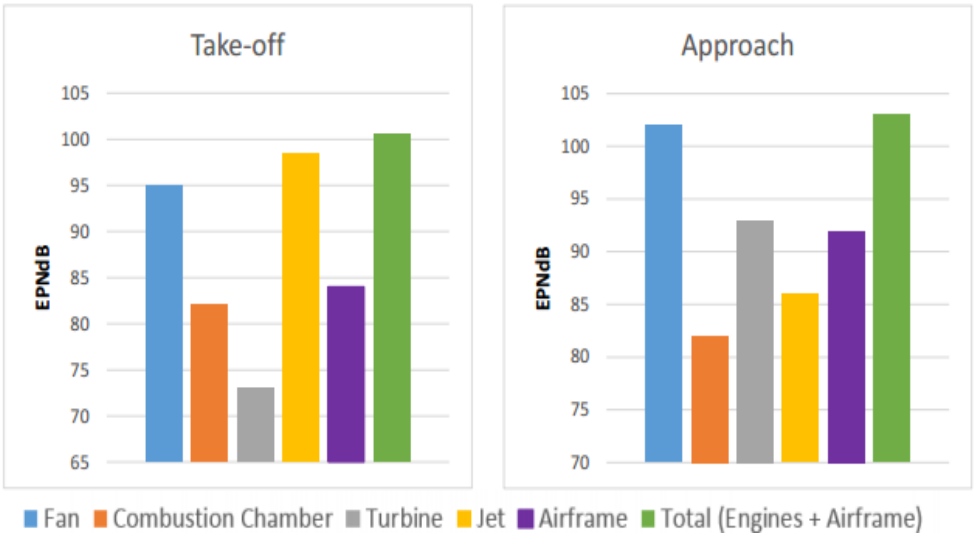

Figure 1.2 Breakdown of aircraft noise sources during take-off and landing [5].

The Unmanned Aerial Vehicles (UAV), also known as drones, represent a new aircraft technology that allows this system to fly without a human pilot on board. UAV

can operate with many degrees of autonomy: either remotely controlled by a human operator, or fully or intermittently autonomously, e.g. by onboard computers. UAVs can fly at an altitude that ranges from several feet to 50,000 feet depending on the type of the UAV. The hand-held type can fly at very low altitudes, which makes the distance between the vehicle and the observer small, leading to an increasein the noise level.

Another factor that can affect the noise level perceiving by the observer is the atmospheric absorption. Mainly if the travel distance is greater, the influence of the atmospheric absorption is eventually more efficient leading to decrease the noise level. Many factors influence the atmospheric absorption such as air temperature, and humidity. Since these machine typically fly short distances, the effect of the atmospheric absorption is negligible. While, over large distances, the sound is led by high frequencies.

Studies have shown that the prediction of flow around thetrailing edge of an airfoil has been an on-going challenge for engineers over the last decades. The complexity of the turbulent flow has led to the use of simplified turbulence models and the development of simplified methods to calculate the noise. However, these assumptions have created difficulties for the design of new airfoils due to their limited accuracy. New advances in computing power provide a much better representation of turbulent flow and therefore open the possibility of designing radically new, quiet airfoil shapes.

1.3 Aims and Objectives

The aim of this research is to numerically investigate the characteristics of the aerodynamic noise radiating from two types of airfoil at different angles of attack, Reynolds number, and Mach number. The results of this thesis can potentially provide

invaluable information to understand the mechanism of noise generation by the flow developing around these airfoils. The objectives of this work are:

- Study the characteristics of the flow around two airfoils: a symmetric airfoil, NACA0012, and a cambered airfoil, CLARKY. This study considers different angles of attack, Reynolds numbers, and Mach numbers.
- Provide results in terms of the sound pressure level spectra and pressure distribution calculated at different probe points located in the far field.
- Provide a better understanding of the flow past an airfoil and the associated aerodynamic sound.

CHAPTER II

LITERATURE REVIEW

2.1 Computational Aeroacoustics Algorithm

The growing demand for better control and reduction of noise has led to the improvement of the accuracy of the aeroacoustics algorithm. The resolution of each aeroacoustics problem can be tackled with the use of different algorithms since every problem exhibits different behaviors and characteristics.

A study by Roe [6] and later by Tam [7] discussed the relevancy of the computational issues in relation to the aeroacoustics problems, including the existence of disparate length scalesbetween acoustic wavelengths and turbulent length scales, the challenges associated with simulating nonlinearities, and the existence of numerical dispersion and dissipationin the spatial and temporal discretizations. The method has to be investigated adequately before the new computational aeroacoustics algorithm is applied to the problem.

There are two main computational aeroacoustics algorithm methods: hybrid and direct. The hybrid method consists of separating the generated noise from the propagation during the process of predicting the noise. It simply calculates the Reynolds stresses by dividing the noise prediction into two parts: aerodynamic and turbulence. This technique that simulates the trailing edge noise may lead to a sensible approach since the splitting

between the fluid and the wave propagation may generate a large scale in both velocity and density.

Many researchers came up with different methods of predicting the turbulent flow and understanding its effects. These methods are: Direct Numerical simulation (DNS), Large Eddy simulation (LES), and Reynolds Averaged Navier Stokes (RANS). The direct numerical simulation is a method that was first studied by Mitchelle et al. in 1992. The aim of this method is to solve the Navier-Stokes equations numerically without any turbulence model to finally provide a description of the flow, and the concomitant sound. First developed by Bechara [1], the Reynolds Averaged Navier Stokes (RANS) method studies the simulation of turbulent flow by producing a time-averaged flow field. In other words, the velocity field is averaged over a time period "t" which is considered to be higher than the time constant of velocity fluctuations. On the other hand, Large Eddy simulation is considered more accurate than RANS it is basically known as a spatial filter rather than averaging.

An analytical noise prediction is used to estimate the noise from transient turbulent flow data. One of the first analytical solutions of Lighthill's acoustic analogy was provided by Ffowcs Williams and Hall [100] for a turbulent diffraction about a semi-infinite half plane. In addition to deriving an analytical Green's method, this method was used to calculate the trailing edge (TE) noise from incompressible LES simulation data by several researchers [101, 102]. In the incompressible LES simulation no coupling is permitted between the fluid dynamics and acoustics since it assumes infinite sound speed in the fluid.

A study by Ffowcs, Williamsand hall [103] reported that changing the shape of the TE, turbulent can be redistributed on small scales which leads to lower noise levels. Using a free space Green's function, the analytical estimation of noise can be obtained theoretically in case a compressible LES is performed. This procedure utilizes Curle'stheory [104]. An extension of Curle's formulation was presented by Ffowcs William Hawkings [105], this equation considers moving noise sources, such as the rotor blade, with respect to the listener.

In the aim of reducing the jet noise, the Lighthill equation is used extensively in acoustic analogies. The equation established by Lighthill has not only contributed in identifying turbulence as the source of the sound, but also has helped in computing the noise produced by subsonic and supersonic flows. An inhomogeneous wave equation was extracted from the Navier-Stokes equations in order to calculate the aerodynamic sound generated from the fluid flow is expressed as follows:

$$\frac{\partial^2 \rho}{\partial t^2} - c^2 \nabla^2 \rho = \frac{\partial^2}{\partial x_i \partial x_j} T_{ij} \tag{2.1}$$

where ρ represents the density, c is the ambient sound speed ($c = \frac{dp}{d\rho}$) , p is the static pressure, and t is the time of the observation.

Lighthill's equation (1) represents the propagation of the wave at a moderate speed of sound c in regards of the aerodynamic noise. The right hand side of the equation represents the acoustic source, and is characterized by the Lighthill's stress tensor defined as follows:

$$T_{ij} = \rho \vartheta_i \vartheta_j - \tau_{ij} + (p' - c^2 \rho')\delta_{ij} \tag{2.2}$$

where the velocity components are $\vartheta_i$and ϑ_j, while δ_{ij} is the Kronecker delta.

Lighthills acoustic analogy (2.1) represents the propagated wave at the speed of sound c in a medium at rest, on which the fluctuating forces are applied on the right hand side of the equation. It physically means that the sound is radiated through the fluctuating internal stresses of a fluid flow, that acts as a stationary and uniform acoustic medium. At the point y in the flow is where the sound pressure level generates, and the observation is at the point x. The exact solution of this equation is expressed as:

$$p(x,t) = \frac{\partial^2}{\partial x_i \partial x_i} \int_V^n \frac{T_{ij}(y, t-\frac{|x-y|}{c})}{4\Pi c^2 |x-y|} \tag{2.3}$$

where V corresponds to the fluid region.

From (2.3) we conclude that the quadrupole source field are generated from the turbulence in a free space. In case the parameters are known, the solution of this equation can be found.

There are extensions of the acoustic analogy of Lighthill, such as the one proposed by Ffowcs Williams and Hawkings [2], where moving solid object can be incorporated into the model. Another approach is the acoustic analogy extension proposed by Kirchhoff [1], applied to low Mach number problems; the acoustic far field is calculated from a time dependent computational fluid dynamics (CFD) solver. The output from the CFD simulation or from a closed-form expression provides information about sound sources using Lighthill's stress tensor.

The Linearized Euler Equations (LEE) solvers have been developed for jet flow [16], and have been further developed [17, 18].The work of Ewert and Schroder [19] has shown limited application to the TE noise; they also developed the Acoustic Perturbation

Equations (APE). APE is known as a special variant of LEE; it leads to minimizing the errors.

The decomposition of the flow variables into mean and perturbed parts is used in the LEE methods.

2.2 Airfoil Self-Noise

The interaction between the boundary layer and the near wake of the airfoil is responsible for the airfoil self-noise generation, known also as trailing edge noise [20]. This phenomenon has been studied by Powell [21], Ffowcs William and Hall [22], Howe [23], and Brooks [20] amongst others.

Brooks [20] presented five airfoil noise mechanisms and found that four produced noise due to the interaction of disturbances with airfoil trailing edge. The one exception is the production through the wing-tip vortex. However, some additional noise sources beside the airfoil trailing edge have been observed recently.

Next, the five mechanisms for airfoil self-noise as classified by Brooks are described.

2.2.1 Turbulent Boundary Layer (TBL) – Trailing edge (TE) Noise

Brooks and Hodgen [24] study showed that the TBL-TE noise that occurs at high Reynolds numbers can be accurately predicted only if the TBL convecting surface pressure field passing the TE is sufficiently know. The TBL settled over an airfoil convects past the trailing edge leading to noise radiation.

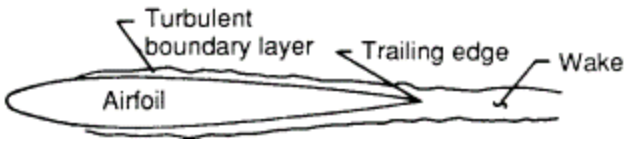

Figure 2.1 Turbulent-Boundary-Layer-trailing-edge-noise

2.2.2 Separation or Stall

The angle of attack is the main source of this noise mechanism. At high angle of attack, the lift coefficient is reduced causing stall at a certain point around the airfoil which leads to an increase in the noise level.

According to Wagner [25], the sound produced from the trailing edge is mainly caused by the flow separation. Whereas for deep stall, noise is radiating from the whole airfoil.

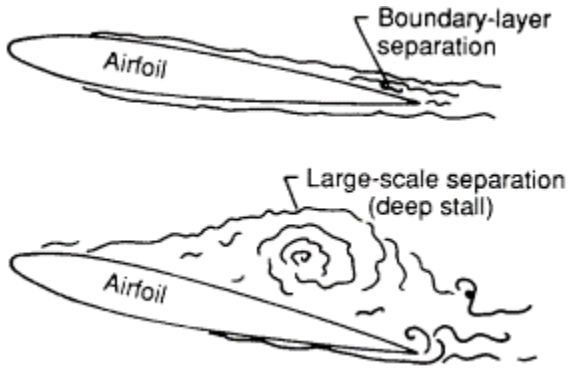

Figure 2.2 Separation-Stall Noise

2.2.3 Laminar-Boundary-Layer (LBL) -Vortex-Shedding (VS)

The vortex shedding occurs when the Laminar Boundary Layer is developed on at least one side of the airfoil. According to Brooks and Marcolini [20], the levels of LBL-VS noise can be normalized at zero angle of attack in order for the transition from LBL-

VS noise to TBL-TE noise to be dependent on Rc. At low Reynolds number, unstable laminar-turbulent transition can occur if the laminar flow regions are extended to the trailing edge. The vortex shedding is coupled with the acoustic waves resulting in tonal noise.

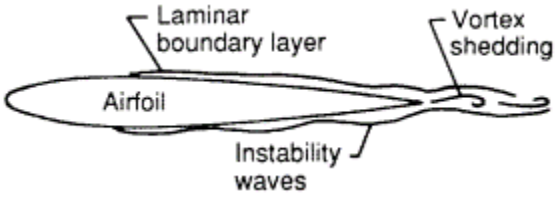

Figure 2.3 Laminar-Boundary-Layer-Vortex-Shedding

2.2.4 Trailing-Edge-Bluntness-Vortex-Shedding-Noise:

According to Brooks and Hodgson [24] it is considered to be an important airfoil-self noise source. This noise mechanism that occurs on the small separation region past an airfoil's blunt trailing edge depends on the bluntness, sharpness of the edge, and Reynolds number.

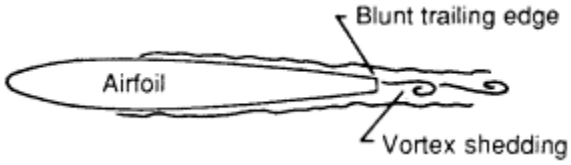

Figure 2.4 Trailing-Edge-Bluntness-Vortex-Trailing-Edge

2.2.5 Tip Vortex Formation Noise

This noise generates a local separated flow near the blade tip, which consists of a vortex with a thick turbulent core. The turbulence passes over the trailing edge of the tip region radiating a trailing edge noise. Brooks Marcolini [20] proposed a study that consist of isolating the tip noise quantitatively and comparing the obtained results for two and three dimensional tests for different conditions.

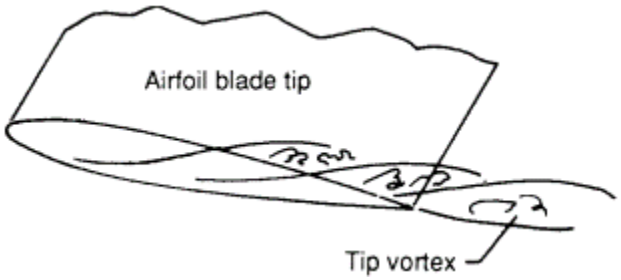

Figure 2.5 Tip Vortex Formation Noise

The trailing edge noise hypothesis demonstrated that it is the main source of the noise which led to three different prediction models. The first model was presented by Lighthill called the Lighthill's acoustic analogy [26] and was then modified by Ffowcs Williams and Hall [22]. Finally, a model by Amiet [27] and Chase [28] consisted of linearizing the hydrostatic equations.

CHAPTER III

GOVERNING EQUATIONS AND NUMERICAL METHODS

3.1 Governing Equations

The Navier-Stokes equations, describing the kinematics and dynamics of a Newtonian viscous fluid in either laminar or turbulent regime, are written in curvilinear coordinates and casted in strong conservation form, with associated initial condition and satisfying certain conditions at the boundaries. The generalized curvilinear coordinate transformation in two-dimensions is written as follows:

$$\tau = \tau(t)$$
$$\xi = \xi(x, y, t) \tag{3.1}$$
$$\eta = \eta(x, y, t)$$

where τ, in this case, represents the physical time, ξ and η are the spatial coordinates in the computational space, and x and y are the spatial coordinates in physical space. In conservative form the equations are written as

$$Q_t + (F_I - F_V)_\xi + (G_I - G_V)_\eta = S_{sponge} \tag{3.2}$$

where the vector of conservative variables is given by

$$Q = \frac{1}{J}\{\rho \quad \rho u \quad \rho v \quad E\}^T \tag{3.3}$$

ρ being the density of the fluid, u and v being the velocity components in physical space, and E the total energy. The inviscid flux vectors, F_I and G_I are defined as

$$F_I = \frac{1}{J}\begin{Bmatrix} \rho U \\ \rho u U + \xi_x P \\ \rho \vartheta U + \xi_y P \\ E U + p\bar{\mathrm{U}} \end{Bmatrix} \tag{3.4}$$

$$G_I = \begin{Bmatrix} \rho U \\ \rho u U + \eta_x P \\ \rho \vartheta U + \eta_y P \\ E V + p\bar{\mathrm{V}} \end{Bmatrix} \tag{3.5}$$

while the viscous flux vectors, F_V and G_V are given as

$$F_V = \frac{1}{J}\begin{Bmatrix} 0 \\ \xi_x \tau_{xx} + \xi_y \tau_{xy} \\ \xi_x \tau_{xy} + \xi_y \tau_{yy} \\ \xi_{y_x} \theta_x + \xi_y \theta_y \end{Bmatrix} \tag{3.6}$$

$$G_V = \frac{1}{J}\begin{Bmatrix} 0 \\ \eta_x \tau_{xx} + \eta_y \tau_{xy} \\ \eta_x \tau_{xy} + \eta_y \tau_{yy} \\ \eta_x \theta_x + \eta_y \theta_y \end{Bmatrix} \tag{3.7}$$

The contravariant velocity components are given as

$$\mathrm{U} = \xi_t + \xi_x u + \xi_y v = \xi_t + \tilde{\mathrm{U}} \tag{3.8}$$

$$\mathrm{V} = \eta_t + \eta_x u + \eta_y v = \eta_t + \tilde{\mathrm{U}} \tag{3.9}$$

The components of the shear stress tensor and heat fluxes are expressed respectively as

$$\tau_{xx} = \frac{2\mu}{3Re}\left[2\left(\xi_x u_\xi + \eta_x u_\eta\right) - \xi_y v_\varepsilon + \eta_y v_\eta\right] \tag{3.10}$$

$$\tau_{yy} = \frac{2\mu}{3Re}\left[2\left(\xi_y v_\xi + \eta_y v_\eta\right) - \xi_x u_\xi + \eta_x u_\eta\right] \tag{3.11}$$

$$\tau_{xy} = \frac{\mu}{Re}\left[2\left(\xi_y u_\xi + \eta_y u_\eta\right) - \xi_x v_\xi + \eta_x v_\eta\right] \tag{3.12}$$

$$\Theta_x = u\tau_{xx} + v\tau_{xy} + \frac{\mu}{(\gamma-1)M^2{}_\infty RePr}\left(\xi_x T_\xi + \eta_x T_\eta\right) \tag{3.13}$$

$$\Theta_y = u\tau_{xy} + v\tau_{yy} + \frac{\mu}{(\gamma-1)M^2{}_\infty RePr}\left(\xi_y T_\xi + \eta_y T_\eta\right) \tag{3.14}$$

S_{sponge}, is the additional source term acting in a sponge layer around the flow domain to damp out the waves exiting the wave. Other notations in the above equations include: p the pressure of the fluid; μ the dynamic viscosity; $\mathrm{Re} = \frac{\rho_\infty V_\infty L}{\mu}$ Reynolds number based on a characteristic velocity, V_∞, density at infinity, ρ_∞, and a characteristic length L; $\mathrm{M}_\infty = \frac{V_\infty}{a}$ Mach number (with a being the speed of sound); PrPrandtl number; and γ the ratio between the specific heats.

The equation of state for an ideal fluid, p = ρRT, is employed to relate the thermodynamic variables (R is the gas constant). The determinant of the Jacobian matrix which is used to transform the equations from the physical space to computational space is denoted by J.

In the above equations, all indices (except the shear stress and heat flux) represent derivatives with respect to the specified argument. All variables are normalized by their respective reference free-stream values, except the pressure which is nondimensionalized by$\rho_\infty {V^2}_\infty$.

3.2 Numerical Methods

Considering a compressible flow, a high-order Navier-Stokes code is applied in this thesis. The time integration is performed using a low dissipation, low dispersion Runge-Kutta scheme [29], while the spatial derivatives are discretized using dispersion relation preserving schemes [30]. A high order spatial filters are used to damp out the unwanted high wavenumber [31]. Nonreflecting boundary conditions are used at the inflow and outflow boundaries [32]. No slip boundary condition is imposed at the solid surface.

With using both low dissipation and low dispersion Runge-Kutta, the time integration is performed. Considering this differential equation:

$$\frac{\partial u}{\partial t} = F(u, t) \tag{3.15}$$

Under the condition of requiring only two storage location per variable, the next equation allows for high order of accuracy with nonlinear operators.

$$\omega_i = \alpha_i \omega_i + \Delta t F(u_{i-1}, t_i) \tag{3.16}$$

$$u_i = u_{i-1} + \beta_i \omega_i \quad For\ i = 1,2, \ldots\ldots, s \tag{3.17}$$

where the known coefficients of the schemes are respectively, α_i, β_i, and $t_i = (n + c_i)\Delta t$, s is the stage number, Δt is the time difference step, $u_0 = u^n$, $u_s = u^{n+1}$, and $w_0 = 0$.

The spatial derivatives are discretized using dispersion relation preserving schemes of Tam and Webb [2] using the following equation:

$$\left(\frac{\partial f}{\partial x}\right) \approx \frac{1}{\Delta x} \sum_{j=-N}^{M} a_j f_{i+j} \tag{3.18}$$

In the aim of damping out the unwanted high wavenumber waves from the solution, the following filter scheme is applied.

$$fi^{(2n)} = \frac{\gamma f_i}{(\Delta x)^{2n}} + a\frac{f_{i+1} - f_{i-1}}{(\Delta x)^{2n}} + b\frac{f_{i+2} - f_{i-2}}{(\Delta x)^{2n}} + c\frac{f_{i+3} - f_{i-3}}{(\Delta x)^{2n}} + d\frac{f_{i+4} - f_{i-4}}{(\Delta x)^{2n}} \tag{3.19}$$

A high order spatial filter was developed by Kennedy and Carpenter [3], the filter vector is then calculated using the following equation:

$$\hat{u} = (1 + \alpha_D \mathbf{D})\mathbf{u} \tag{3.20}$$

where the filter vector is$\hat{u}$**,** $\mathbf{D}$ is the filter matrix, and $\alpha_D = (-1)^{n+1} 2^{-2n}$.

Nonreflecting boundary conditions are used at the inflow and outflow boundaries (Kim and Lee [5]). In order to avoid the nonphysical wave to reflect back into the domain

special care is taken at the inflow and outflow. The amplitude of the incoming wave and the imposed far field variables are used to determine the boundaries flow conditions. Three characteristics are entering the domain and one is leaving for the inflow case. By imposing the velocity and pressure far upstream and considering the inlet plane far from the disturbances, the inflow can then be considered isentropic.

The amplitude of the incoming characteristic waves at the inflow are expressed as follows:

$$L_1 = 0$$

$$L_2 = k_{in}\frac{v - v_\infty}{2} \tag{3.21}$$

$$L_3 = k_{in}[(u - u_\infty) + \frac{p - p_\infty}{\rho c}]$$

where ρ is the density, c is the speed of sound, and k_{in} is expressed as

$$k_{in} = \sigma_{in}(1 - M_{max}^2)\frac{c}{l} \tag{3.22}$$

where σ_{in} is a known coefficient that controls the partial reflexivity at the inlet, M_{max} is the Mach number in the flow at the maximum, l is the length of the domain.

On the other hand, three characteristics waves are leaving the domain as one enters at the outflow. Only the pressure is imposed far downstream, and can be calculated at the outlet using the amplitude of the leaving wave L_4 .

$$L_4 = K_{out}\frac{p - p_\infty}{\rho c} \tag{3.23}$$

where c is the speed of sound and K_{out} is expressed as:

$$K_{out} = \sigma_{out}(1 - M_{max}^2)\frac{c}{l} \tag{3.24}$$

where σ_{out} is the density at the outlet, M_{max} is the Mach number in the flow at the maximum, c is the speed of sound, and l is the length of the domain.

The amplitude of the characteristics waves L_1, L_2,L_3 are calculated from the interior points, while the characteristic wave L_4 is calculated from exterior points.

Moreover, no slip boundary condition is imposed at the solid surface, $u_{wall} = v_{wall} = 0$.

CHAPTER IV

RESULTS AND DISCUSSION

In this chapter, the results of various numerical simulations are presented and discussed. First, contour plots of the characteristics of the flow past two different airfoils at various angle of attack, Reynolds numbers, and Mach numbers are presented. Then, results for the sound pressure level spectra calculated from a probe point in the far field are presented and discussed.

4.1 Procedures

In this study, two different airfoils are considered:a symmetric airfoil, NACA0012, and a cambered airfoil CLARKY.The effect of changing the profile of the airfoil on the characteristics of the flow will be discussed. The results are obtained using three different Angle of Attack (AOA) of 0°, 6°, and 12°, respectively, two different Reynolds numbers (Re), 50000 and 100000, respectively, and two different Mach number (Ma) 0.2 and 0.4, respectively.

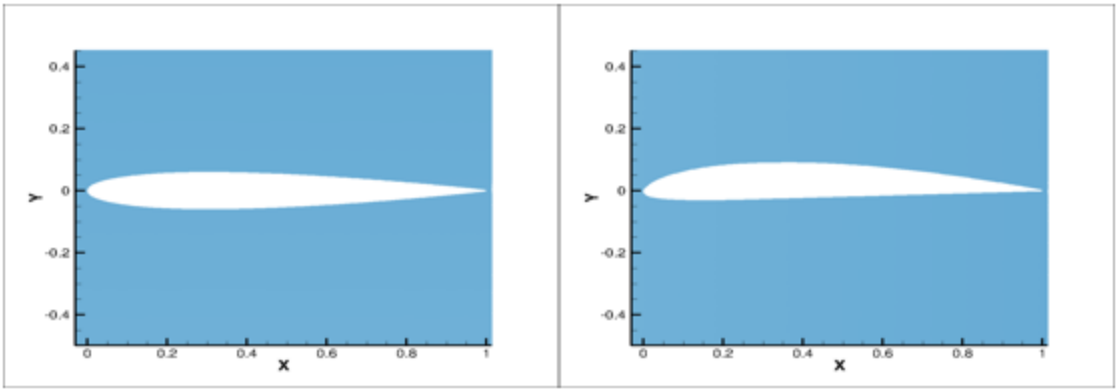

Figure 4.1 Airfoil types

(a) NACA 0012 profile using TECPLOT 360, (b) CLARKY profile using TECPLOT 360

Figure 4.1 represents the profiles of the two different airfoils used to this study. The NACA 0012 airfoil is symmetric, (00 in the nomenclature is indicating that the airfoil has no camber). The next two digits in its nomenclature indicated that the airfoil has a 12% of thickness from chord. Analytically, the formula of the shape of NACA 0012 can be presented as follows:

$$y_t = 5t_c\left[0.2696\sqrt{\frac{x}{c}} + (-0.1260)\left(\frac{x}{c}\right) + (-0.3516)\left(\frac{x}{c}\right)^2 + 0.2843\left(\frac{x}{c}\right)^3 + (-0.1015)\left(\frac{x}{c}\right)^4\right] \quad (4.1)$$

where c refers to the chord length, x is the position along the chord from 0 to z. Y_t represents the half thickness at a given value of x (centerline to surface), and t_c is the maximum thickness as a function of the chord.

CLARKY is a cambered type of profile; it has thickness of 11.7%,is flat on the lower surface from 30 percent of chord back. The flat bottom simplifies angle measurements on propellers, and makes for easy construction of wings on a flat surface.

In Fig 4.2, two grid topologies for the different airfoil profiles are presented (the number of grid points is 230,764 for the NACA airfoil, and 216,162 for the CLARKY

airfoil). For both airfoils, the grid spacing is decreased near the wall, and in the vicinity of the trailing edge and the leading edge; stretching is used in the farfield to minimize the reflection of spurious waves from the farfield boundaries.

(a)

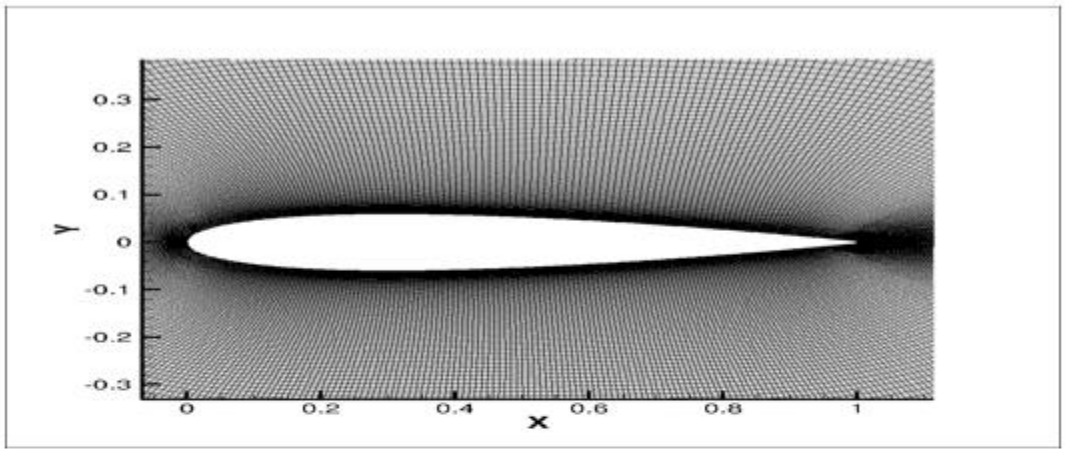

(b)

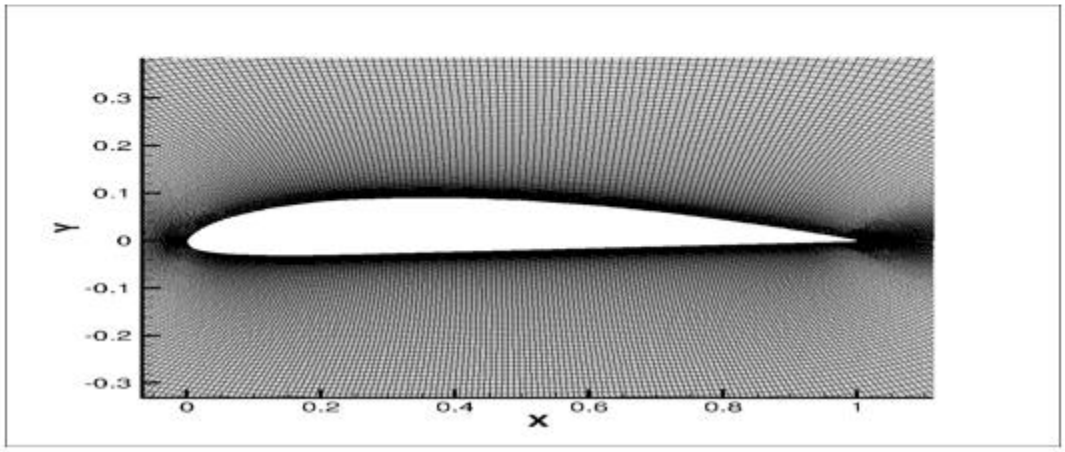

Figure 4.2 Airfoil grid type

(a) NACA 0012 grid topology using TECHPLOT 360, (b) CLARKY grid topology using TECHPLOT 360.

Results representing the characteristic of the flow past the airfoil and the radiated sound in terms of pressure are plotted and discussed. The comparison between the different cases, where the airfoils profile, the angle of attack, Reynolds number, and Mach number are varied, in terms of pressure and sound pressure level is discussed. At a probe location of coordinates x= 3.53 and y=7.40 chord units, away from the airfoil, the noise is calculated and time history pressure plots are presented and discussed.

The 24 run cases performed in this study are given in tables 4.1, 4.2, 4.3, 4.4, 4.5, and 4.6.

Table 4.1 Run cases for NACA 0012 of AOA=0°.

Case number	Reynolds number	Mach number
1	50,000	0.2
2	50,000	0.4
3	100,000	0.2
4	100,000	0.4

Table 4.2 Run cases for NACA 0012 of AOA= 6°.

Case number	Reynolds number	Mach number
5	50,000	0.2
6	50,000	0.4
7	100,000	0.2
8	100,000	0.4

Table 4.3 Run cases for NACA 0012 of AOA=12°.

Case number	Reynolds number	Mach number
9	50,000	0.2
10	50,000	0.4
11	100,000	0.2
12	100,000	0.4

Table 4.4 Run cases for CLARKY of Angle of Attack 0°.

Case number	Reynolds number	Mach number
13	50,000	0.2
14	50,000	0.4
15	100,000	0.2
16	100,000	0.4

Table 4.5 Run cases for CLARKY of AOA=6°.

Case number	Reynolds number	Mach number
17	50,000	0.2
18	50,000	0.4
19	100,000	0.2
20	100,000	0.4

Table 4.6 Run cases for CLARKY of AOA=12°.

Case number	Reynolds number	Mach number
21	50,000	0.2
22	50,000	0.4
23	100,000	0.2
24	100,000	0.4

4.2 Pressure Contour Plots

The following figures represent the characteristic of the flow past the airfoil, including the acoustic waves propagating to the farfield., for two airfoil profiles, three angles of attack, two Reynolds numbers, and two Mach number, as given in tables 4.1, 4.2, 4.3, 4.4, 4.5, and 4.6. Fig 4.3 and 4.4 show that at low Reynolds number, the flow about airfoil has a different characteristic from that found at high Reynold number. For a 0° angle of attack and Re=50,000, a laminar boundary layers forms initially on the airfoil surface, and a small region of separation appears in the vicinity of the trailing edge. As Reynolds number become larger, the acoustic waves traveling from the airfoil to the far field become more intense and larger scales of vortices are produced near the trailing edge. Also, increasing the Mach number leads to more intense acoustic waves that travel to both upstream and downstream of the far field.

Fig 4.5, 4.6, 4.7, 4.8 shows the effect of changing the angle of attack on the characteristic of the flow and sound about the airfoil. When the angle of attack is non-zero (either 6 or 12 degree), the flow starts to separate from the airfoil, generating vortices that travel downstream (vortices are highlighted by spots of hydrodynamic

pressure in the wake). These vortices are responsible for the acoustic waves that are generated.

Fig 4.9 and 4.10 shows that at 0° angle of attack, low Reynolds number and Mach number, the flow around a cambered airfoil starts to separate and the acoustic waves and vortices are more intense than the flow around a symmetric airfoil.

Increasing the Reynolds number and Mach number while keeping the angle of attack at 0° leads to the generation of more intense acoustic waves and vortices. Fig 4.11, 4.12, 4.13, and 4.14 demonstrates that a non-zero angle of attack for a cambered airfoil generates larger vortices and more turbulence intensity compare to a symmetrical airfoil.

In the appendix, plots of the acoustic pressure history for different angle of attack, Reynolds number, and Mach number are included. The acoustic pressure is taken from a probe location of coordinates x= 3.53 and y=7.40 chord units, away from the airfoil.

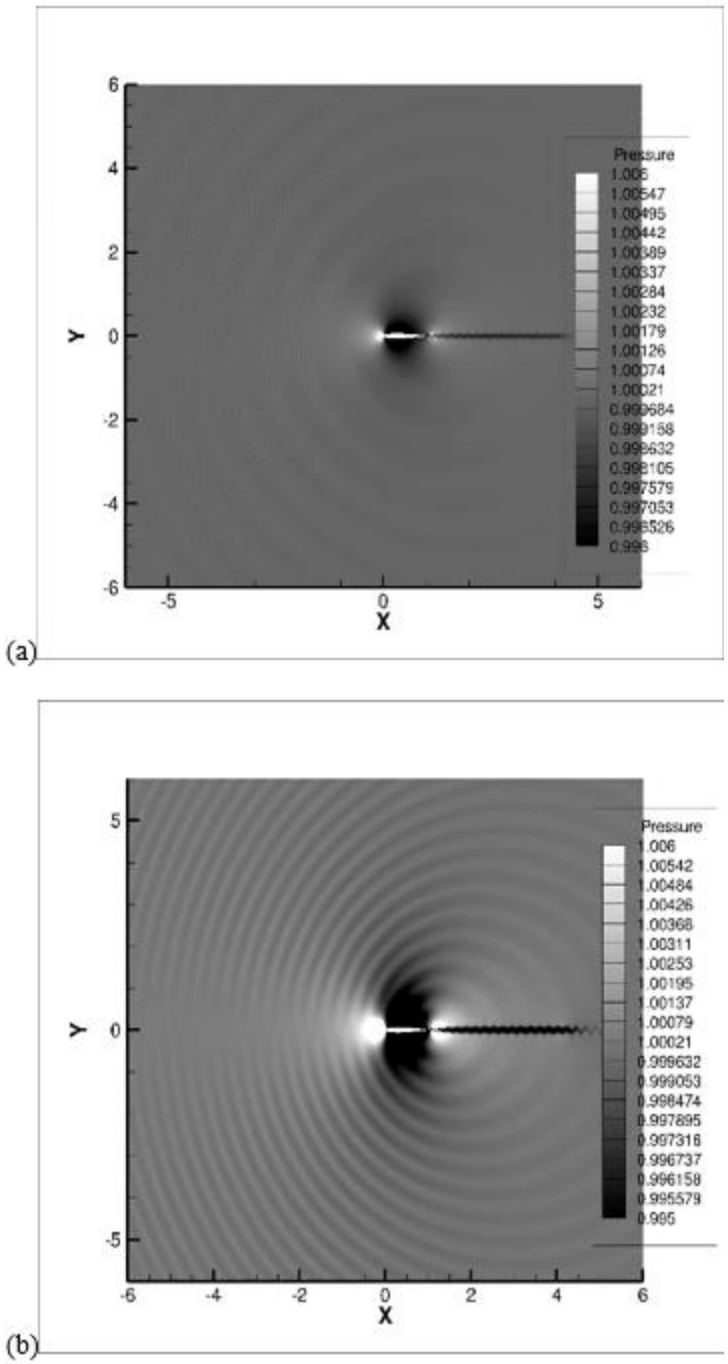

Figure 4.3 Pressure contour plots for NACAA 0012 of AOA=0°, Re=50,000, and (a) Ma=0.2 (b) Ma=0.4

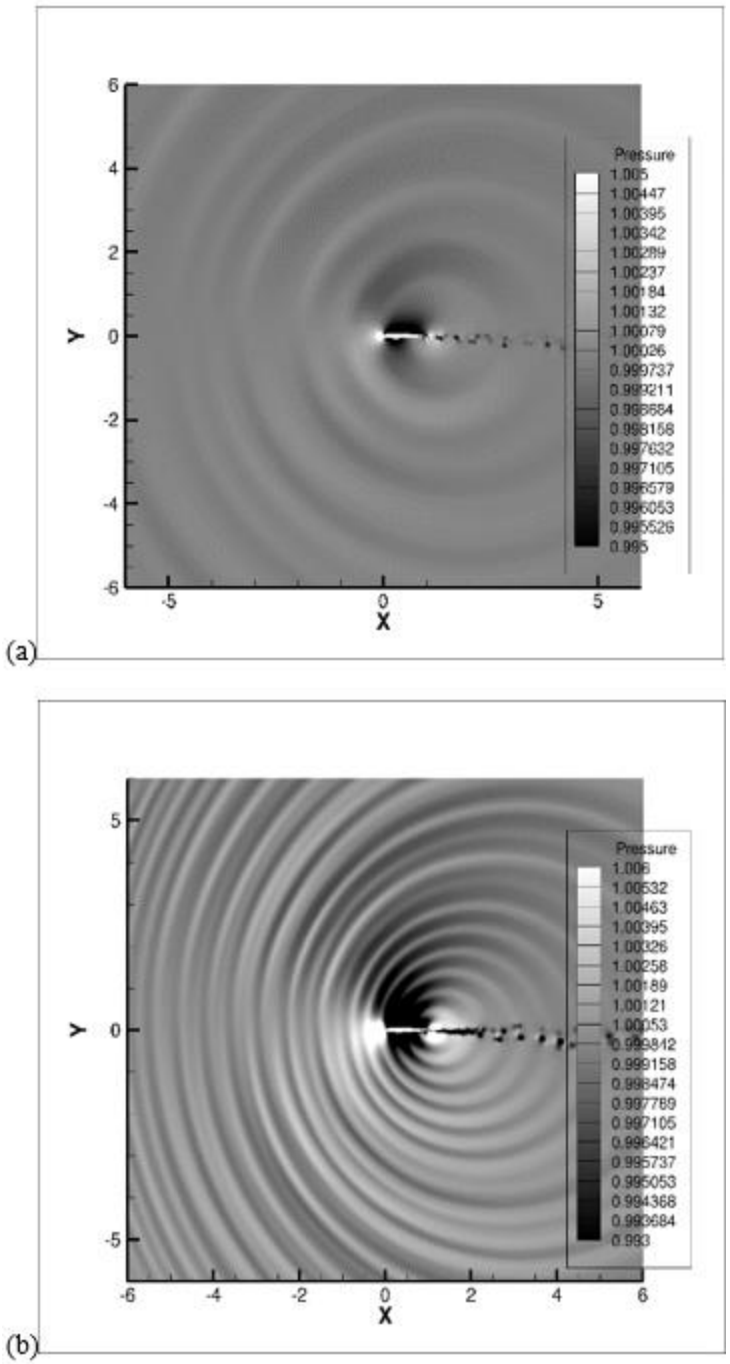

Figure 4.4 Pressure contour plots for NACAA 0012 of AOA=0°, Re=100,000, and (a) Ma=0.2 (b) Ma=0.4.

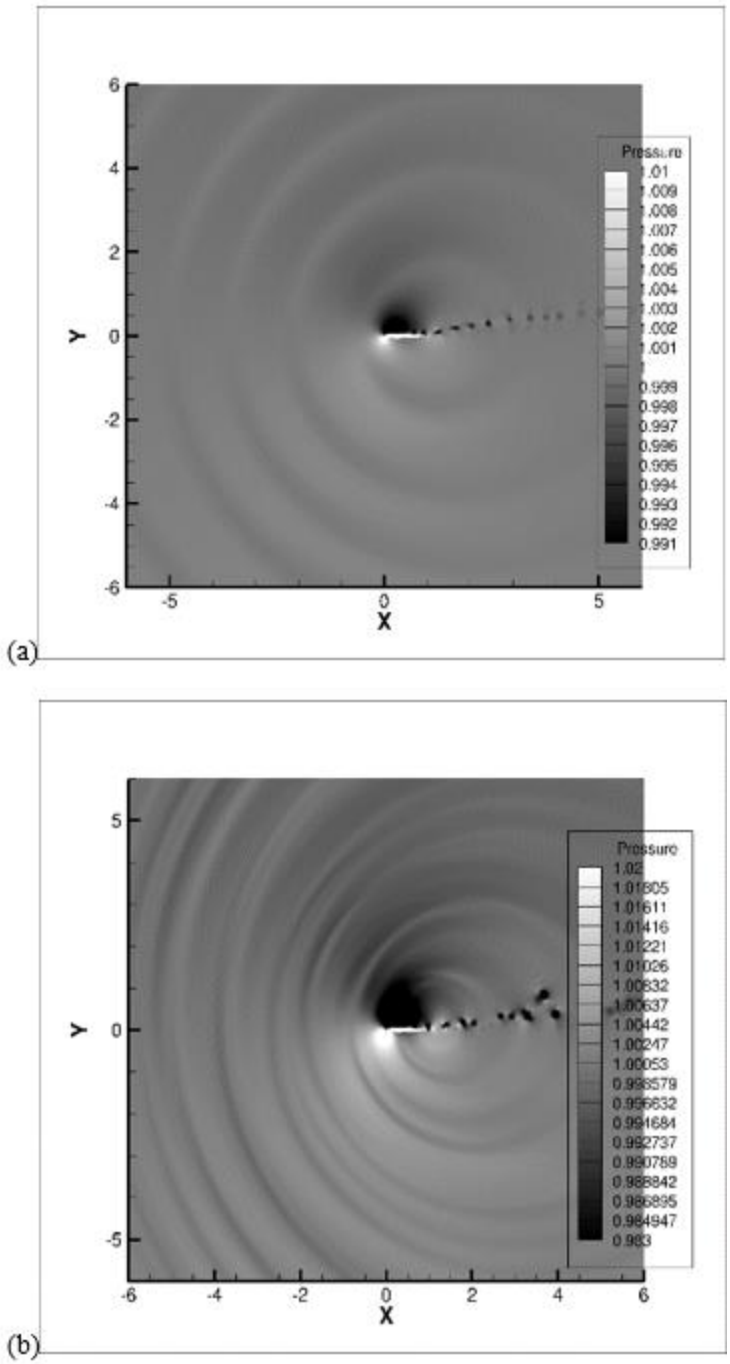

Figure 4.5 Pressure contour plots for NACAA 0012 of AOA=6°, Re=50,000, and (a) Ma=0.2 (b) Ma=0.4.

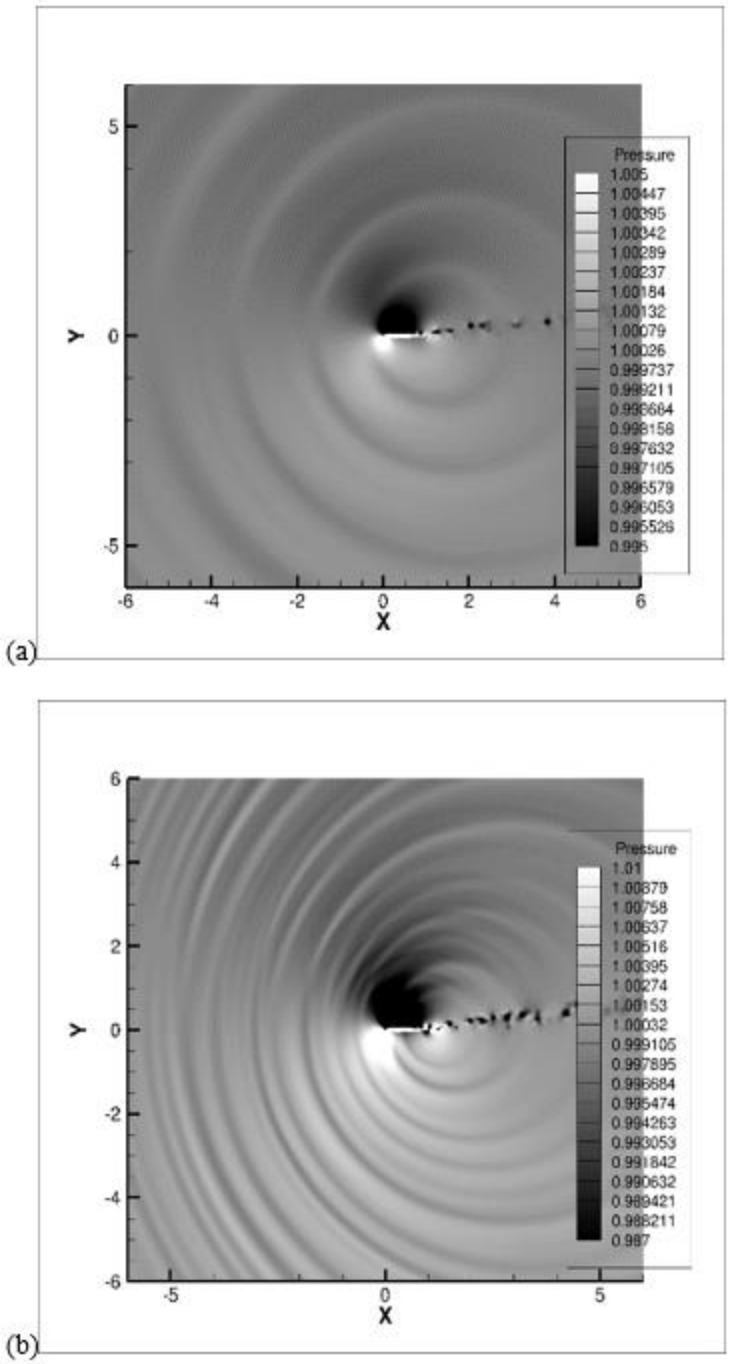

Figure 4.6 Pressure contour plots for NACAA 0012 of AOA=6°, Re=100,000, and (a) Ma=0.2 (b) Ma=0.4.

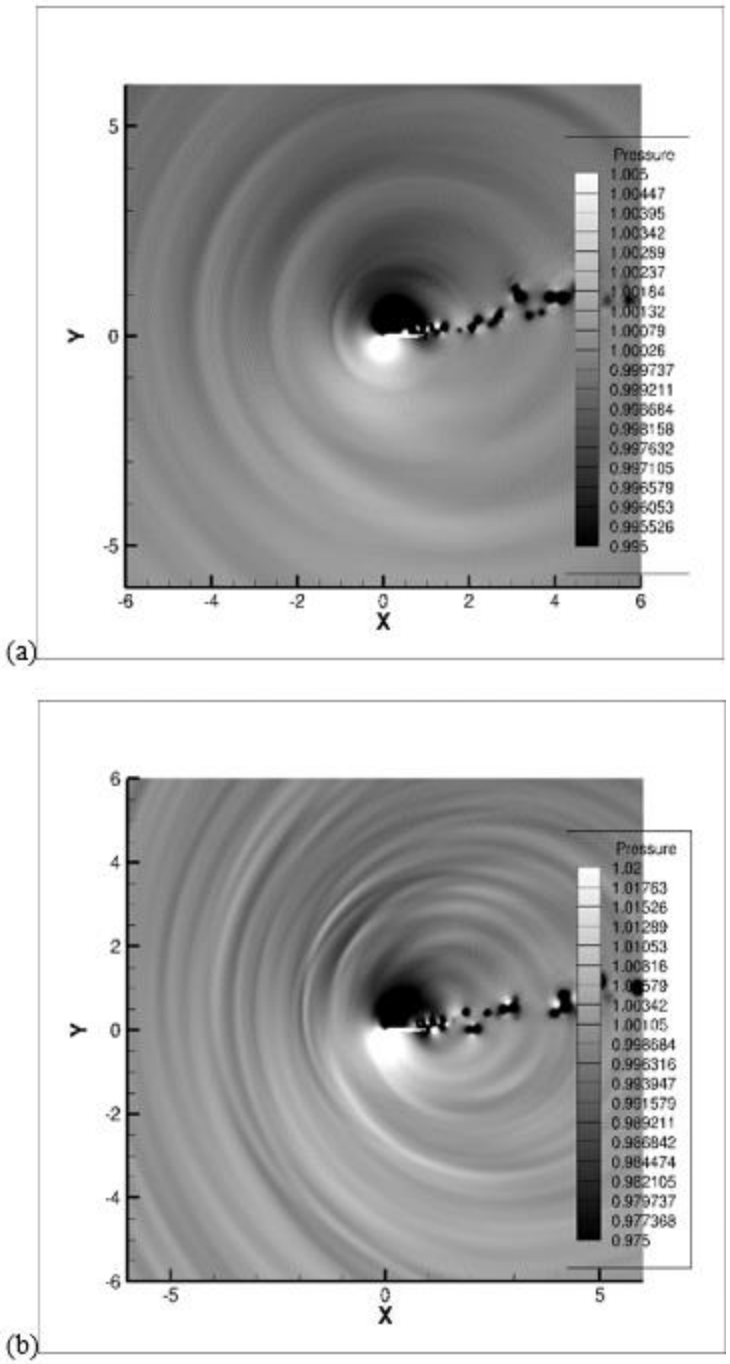

Figure 4.7 Pressure contour plots for NACAA 0012 of AOA=12°, Re=50,000, and (a) Ma=0.2 (b) Ma=0.4.

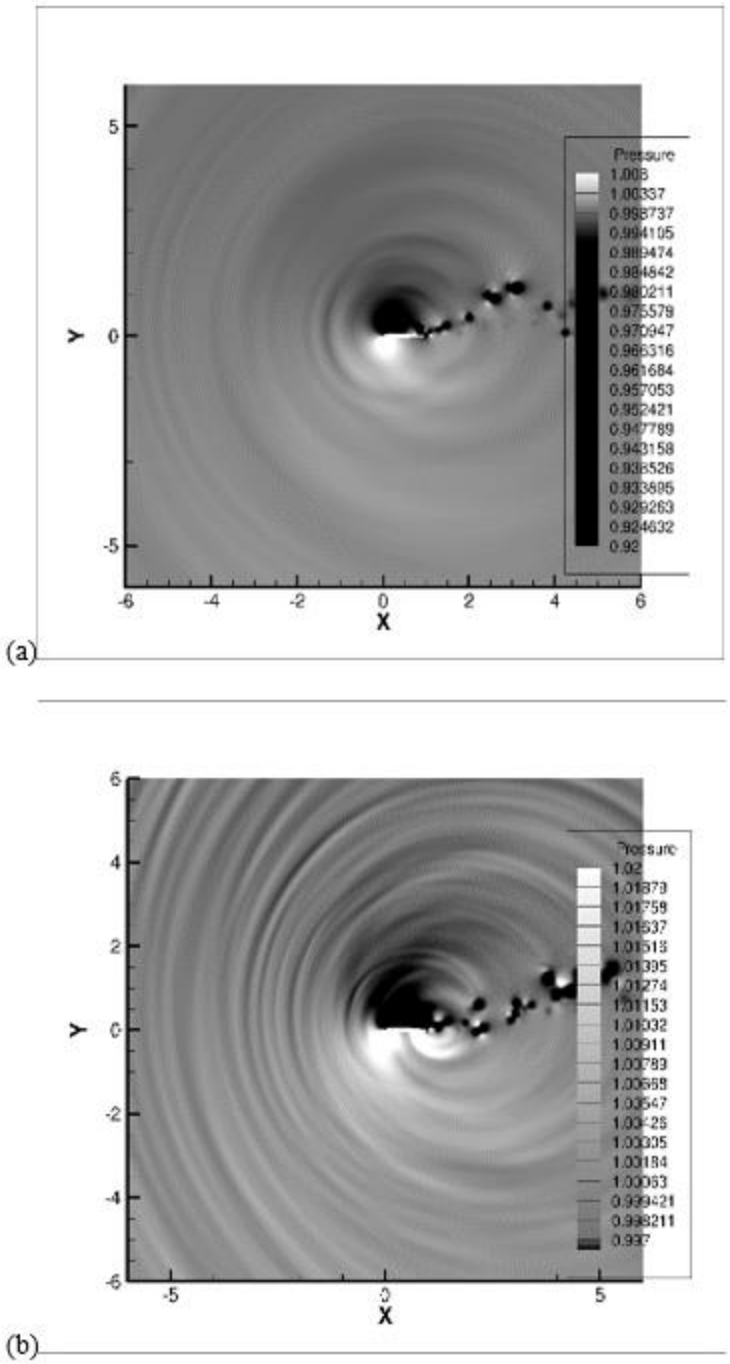

Figure 4.8 Pressure contour plots for NACAA 0012 of AOA=12°, Re=100,000, and (a) Ma=0.2 (b) Ma=0.4.

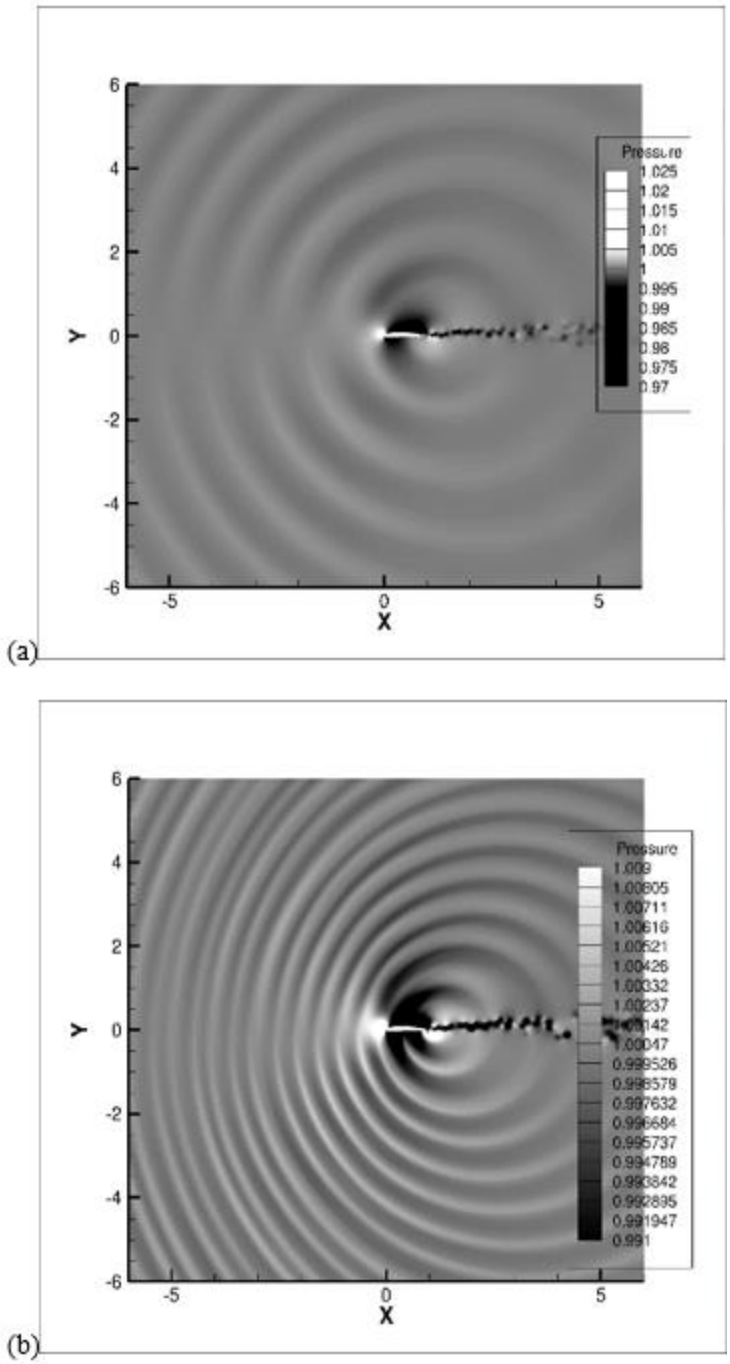

Figure 4.9 Pressure contour plots for CLARKY of AOA=0°, Re=50,000, and (a) Ma=0.2 (b) Ma=0.4.

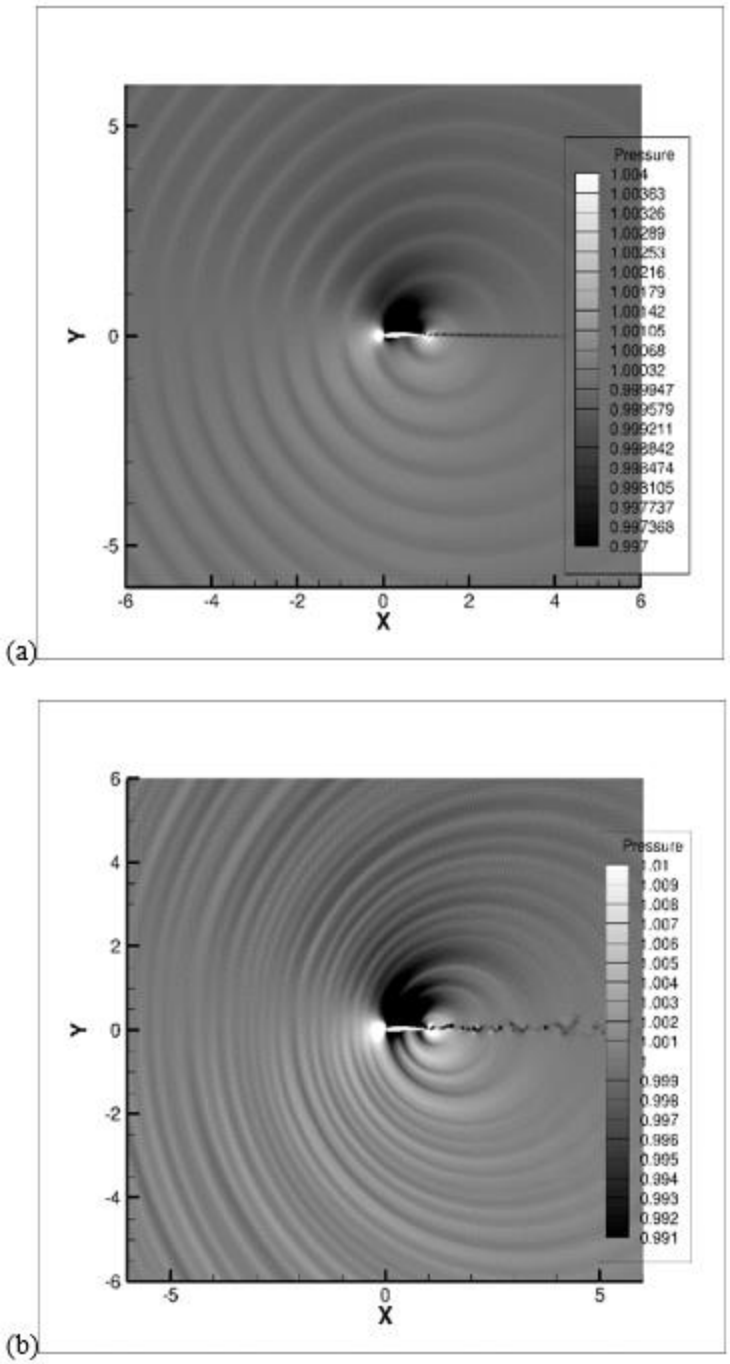

Figure 4.10 Pressure contour plots for CLARKY of AOA=0°, Re=100,000, and (a) Ma=0.2 (b) Ma=0.4.

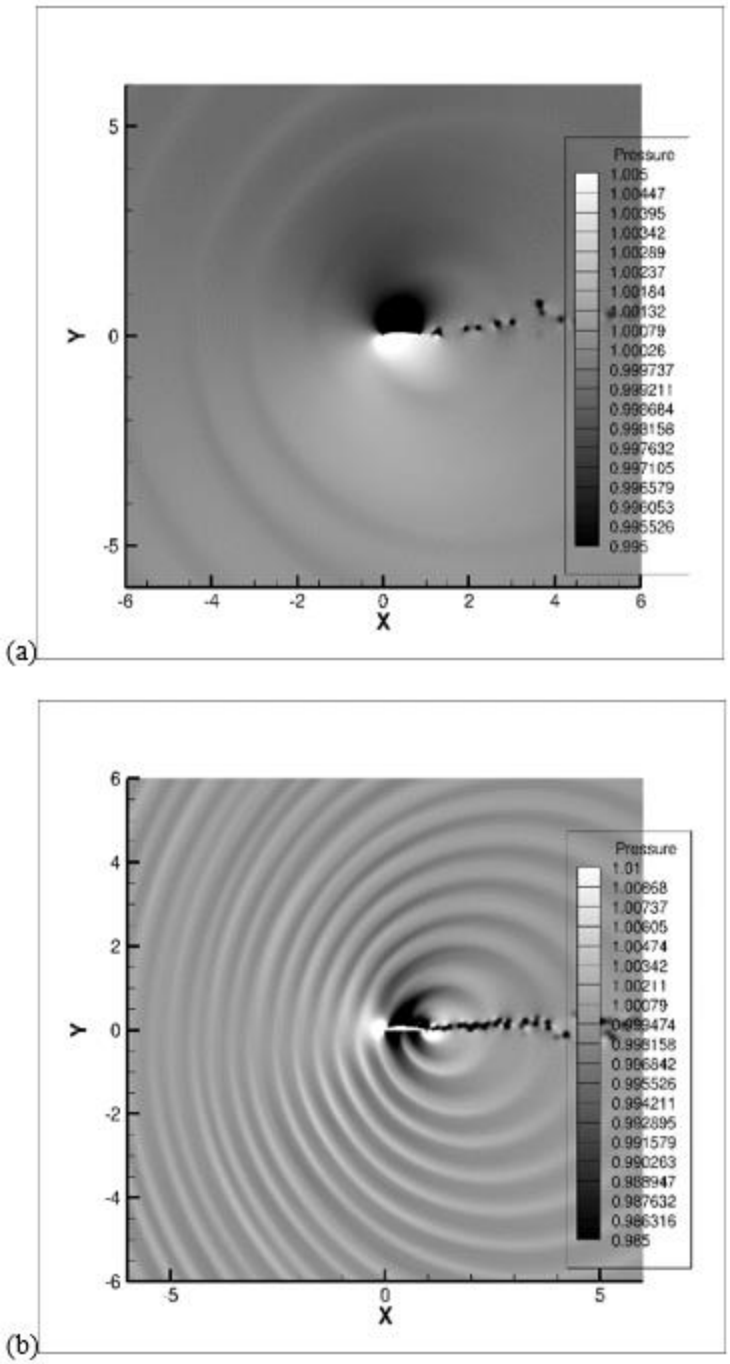

Figure 4.11 Pressure contour plots for CLARKY of AOA=6°, Re=50,000, and (a) Ma=0.2 (b) Ma=0.4.

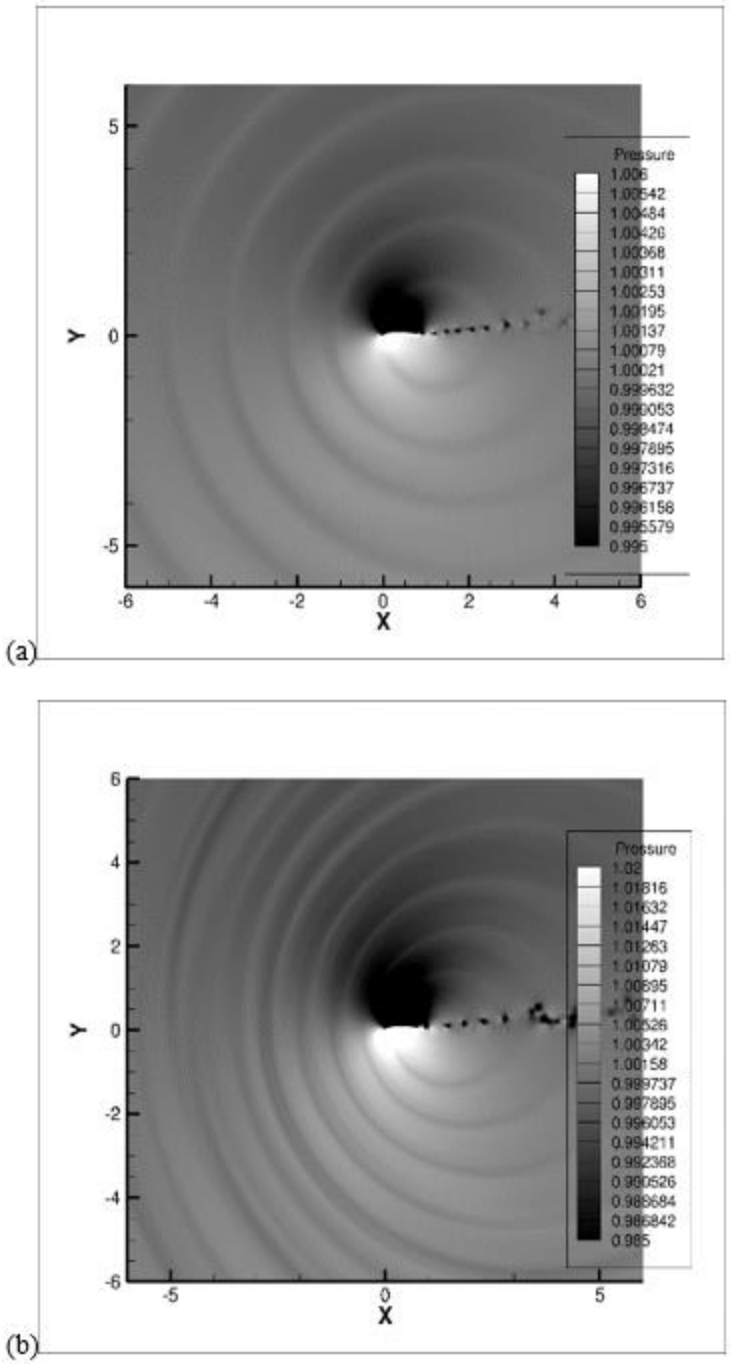

Figure 4.12 Pressure contour plots for CLARKY of AOA=6°, Re=100,000, and (a) Ma=0.2 (b) Ma=0.4.

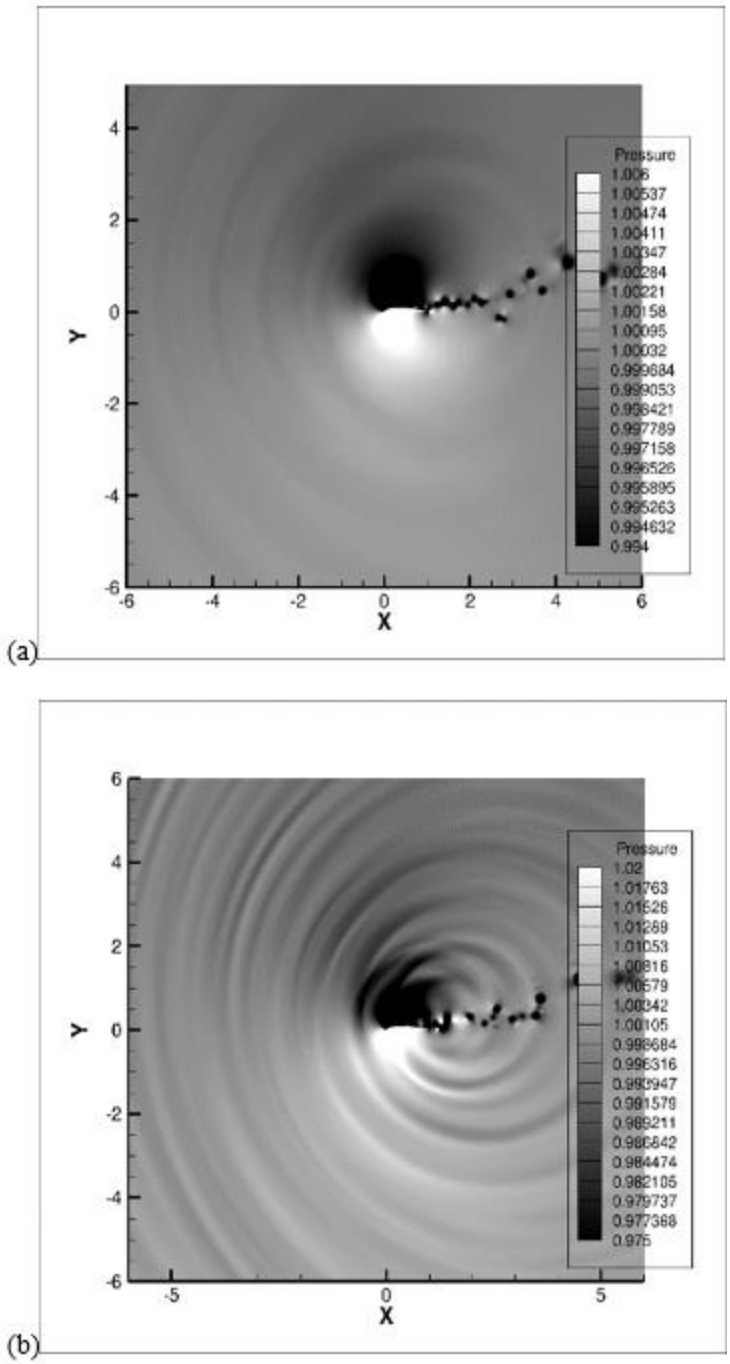

Figure 4.13 Pressure contour plots for CLARKY of AOA=12°, Re=50,000, and (a) Ma=0.2 (b) Ma=0.4.

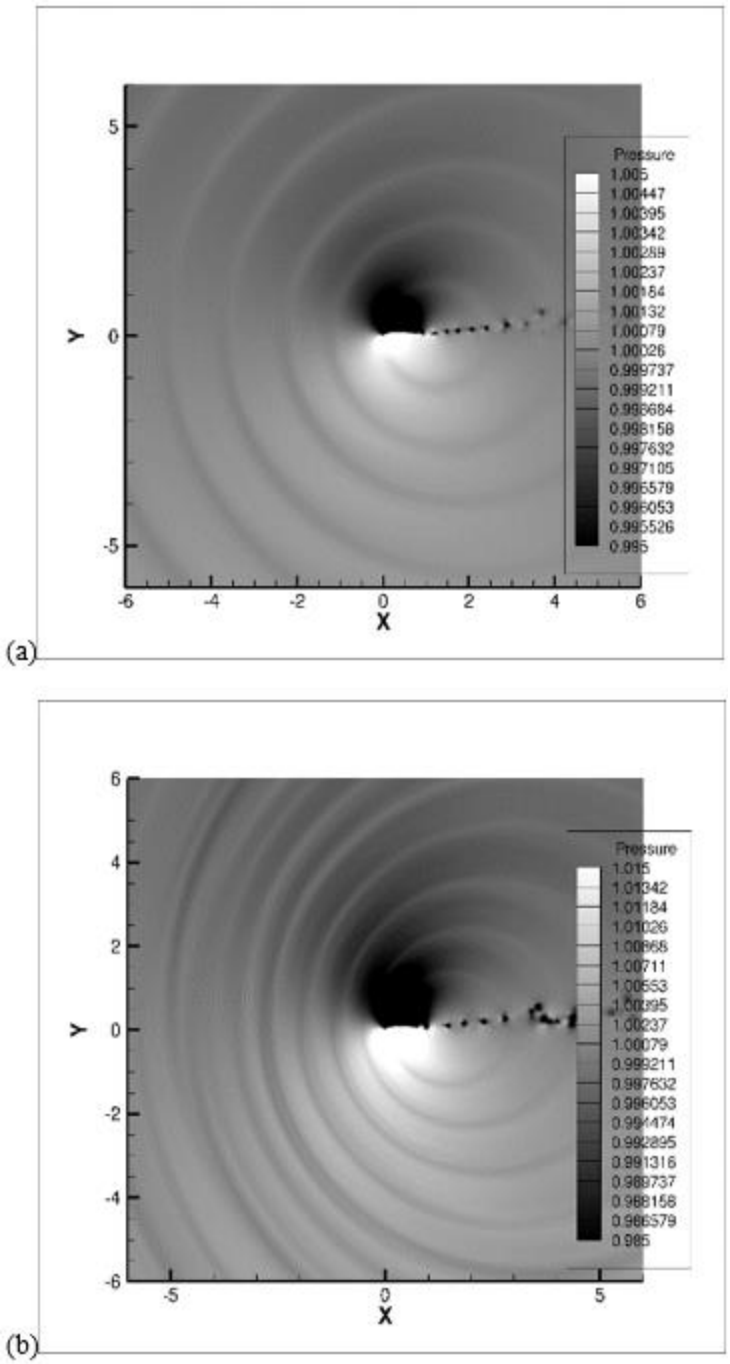

Figure 4.14 Pressure contour plots for CLARKY of AOA=12°, Re=100,000, and (a) Ma=0.2 (b) Ma=0.4.

4.3 Sound Pressure Level Spectra Plots

The following figures represent the sound pressure level spectra (SPL) versus the Strouhal number (St) of both NACA 0012 and CLARKY for the same Reynolds number and Mach number, and at different angles of attack. These figures give the frequency representation of SPL, including the peak frequency which is important in identifying any existing tone noise in the data. Fig 4.15 shows that for 0° angle of attack and Ma=0.2, the the maximum SPL=52 dB, and for 12° angle of attack and Ma=0.2, the maximum SPL=73 dB. Fig 4.16 shows that for 0° angle of attack and Ma=0.4, the maximum SPL=64 dB, and for 12° angle of attack and Ma=0.4, the maximum SPL=91 dB.

When increasing the angles of attack and Mach number the Sound Pressure level increases as the Strouhal number decreases. Since increasing the angle of attack enlarges the intensity of the wake, wherein vortices are larger (as a result of the flow separation), this leads to an increase in the amplitude of the acoustic waves (SPL is higher).

Fig 4.18 and 4.19 shows the effect of the Reynolds number as the Angle of Attack is increased. In Fig 4.19, for 0° angle of attack and Ma=0.2, the SPL=70 dB. For 12° angle of attack and Ma=0.2, the maximum SPL=80 dB. The increase of the Reynolds number leads to an increase in the SPL as the Strouhal number decreases.

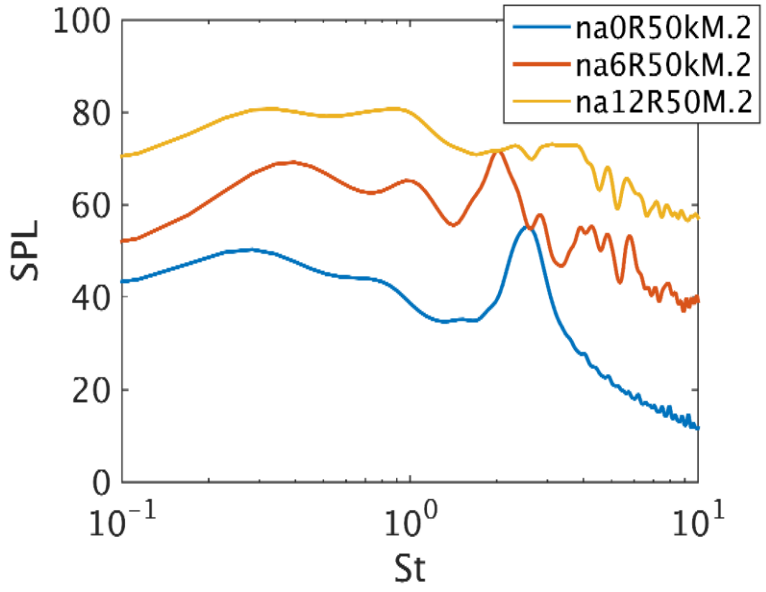

Figure 4.15 SPL vs St for NACA 0012 of AOA=0°, AOA=6°, AOA=12°, for Re=50,000, Ma=0.2.

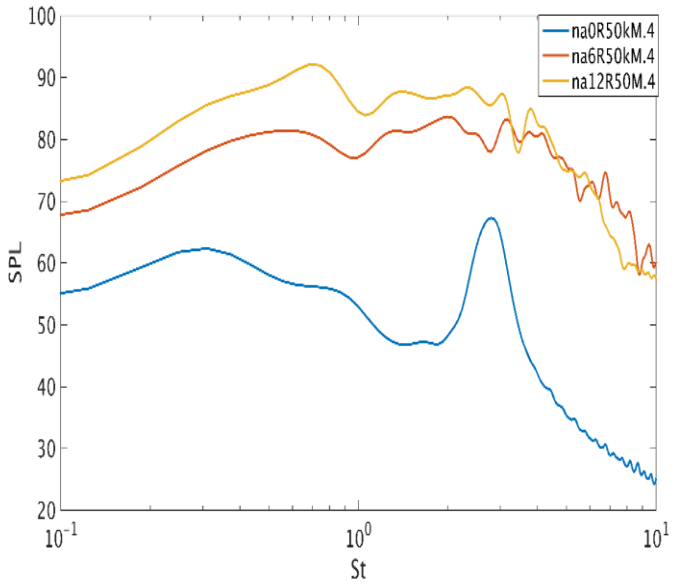

Figure 4.16 SPL vs St for NACA 0012 of AOA=0°, AOA=6°, AOA=12°, for Re=50,000, Ma=0.4.

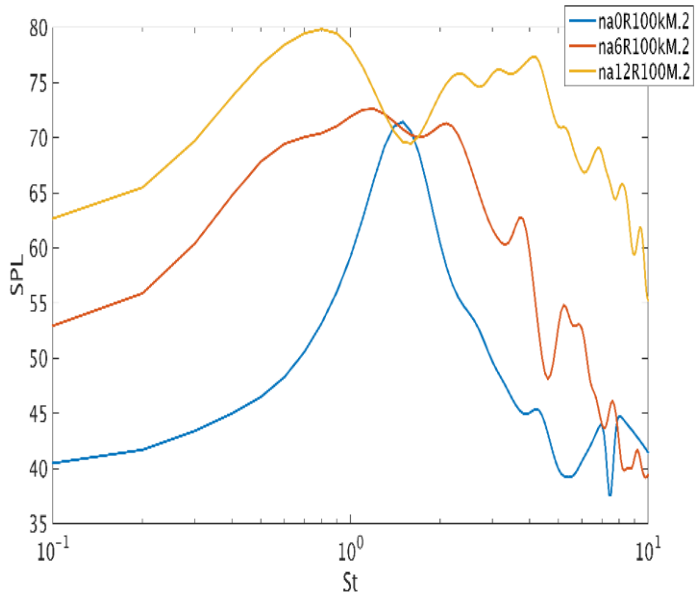

Figure 4.17 SPL vs St for NACA 0012 of AOA=0°, AOA=6°, AOA=12°, for Re=100,000, Ma=0.2.

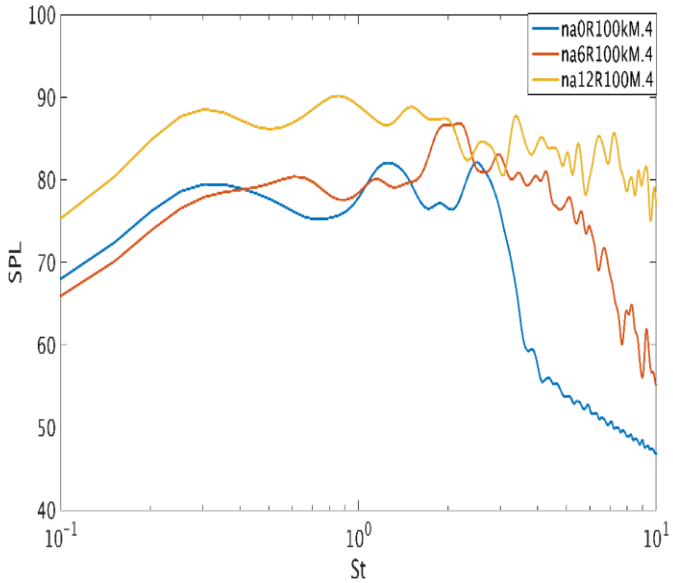

Figure 4.18 SPL vs St for NACA 0012 of AOA=0°, AOA=6°, AOA=12°, for Re=100,000, Ma=0.4.

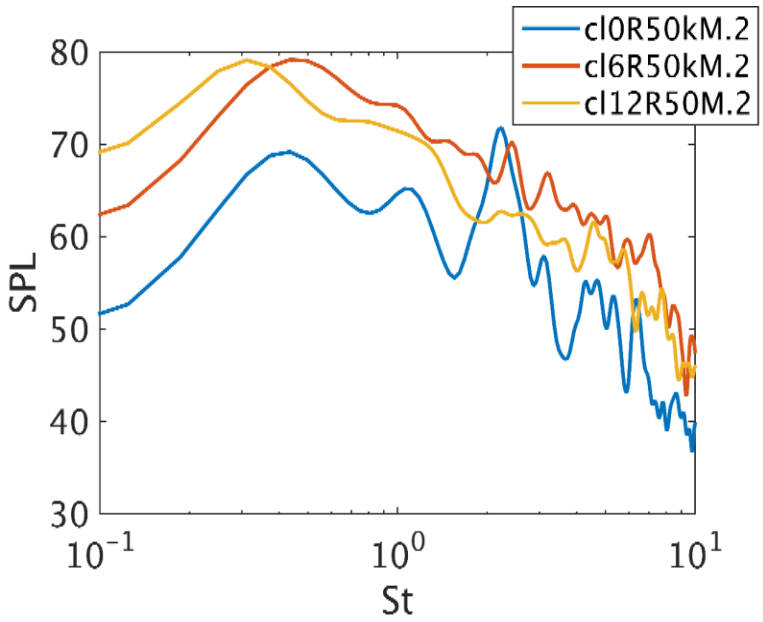

Figure 4.19 SPL vs St for CLARKY of AOA=0°, AOA=6°, AOA=12°, for Re=50,000, Ma=0.2.

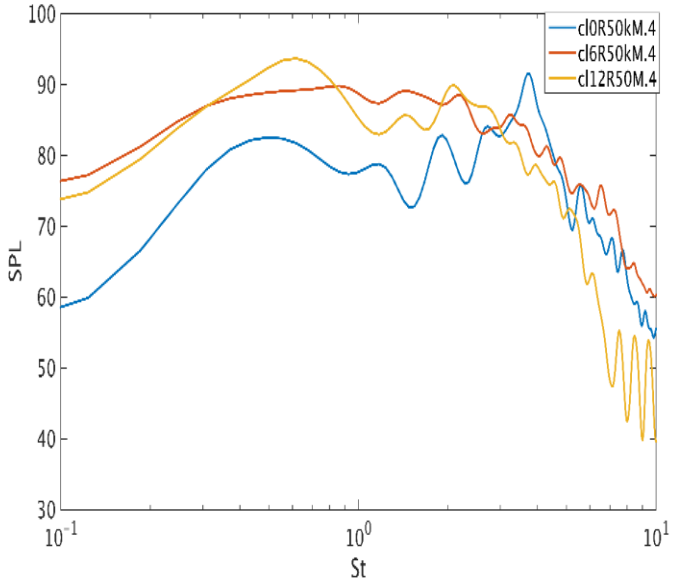

Figure 4.20 SPL vs St for CLARKY of AOA=0°, AOA=6°, AOA=12°, for Re=50,000, Ma=0.4.

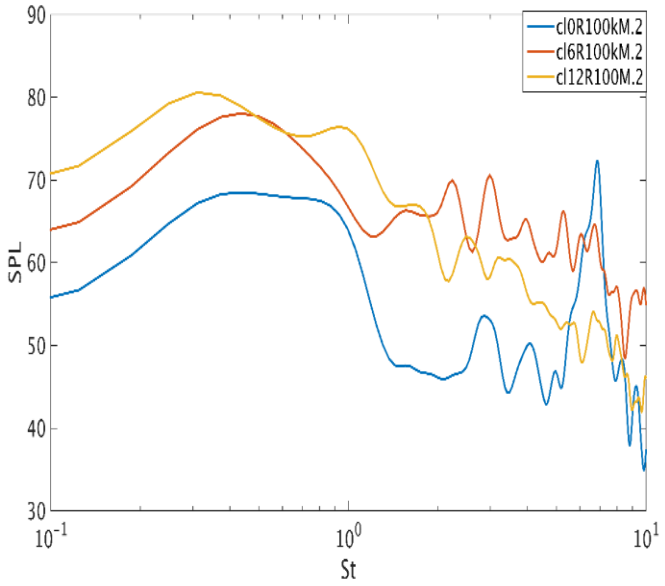

Figure 4.21 SPL vs St for CLARKY of AOA=0°, AOA=6°, AOA=12°, for Re=100,000, Ma=0.2.

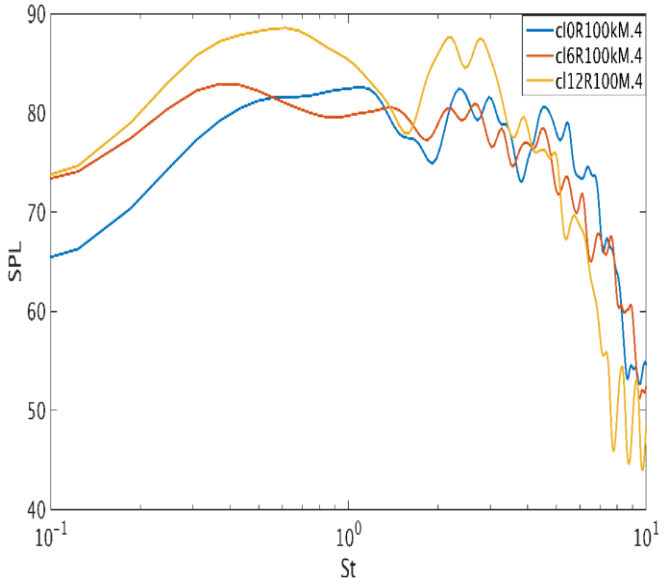

Figure 4.22 SPL vs St for CLARKY of AOA=0°, AOA=6°, AOA=12°, for Re=100,000, Ma=0.4.

The following figures represent the sound pressure level spectra (SPL) versus the Strouhal number (St) of both NACA 0012 and CLARKY for the same Reynolds number, at the same Angle of Attack, and for different Mach numbers. They all show that by increasing the Mach number, the SPL increases considerably (by more than 10 dB in some cases).

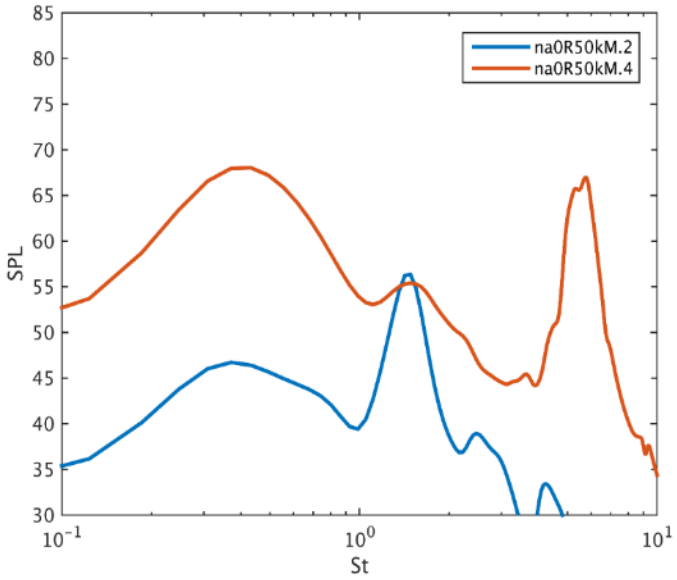

Figure 4.23 SPL vs St for NACA0012 at AOA= 0°, Re=50,000, Ma=0.2 and Ma=0.4.

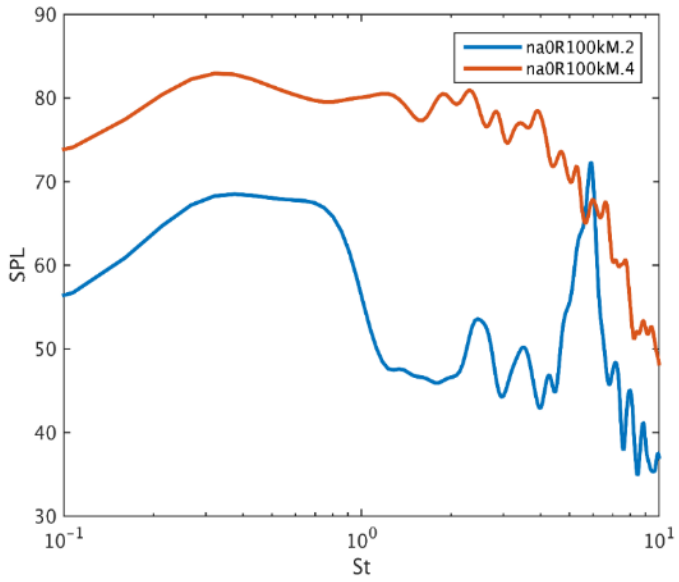

Figure 4.24 SPL vs St for NACA0012 at AOA= 0°, Re=100,000, Ma=0.2 and Ma=0.4.

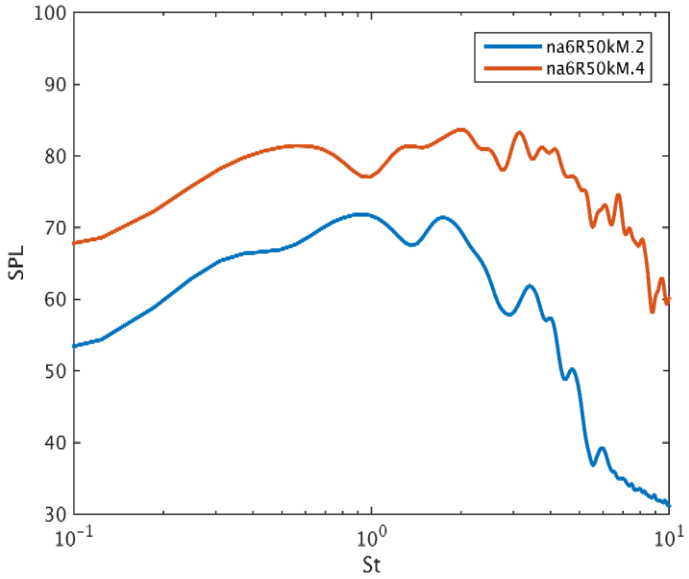

Figure 4.25 SPL vs St for NACA0012 at AOA= 6°, Re=50,000, Ma=0.2 and Ma=0.4.

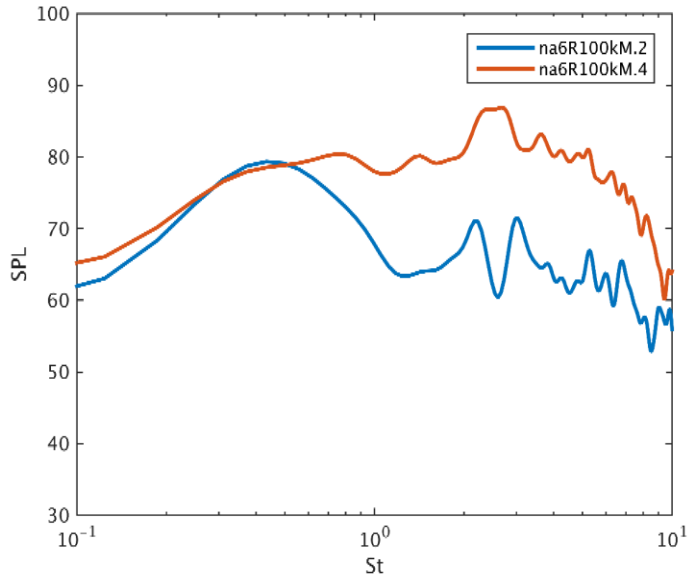

Figure 4.26 SPL vs St for NACA0012 at AOA= 6°, Re=100,000, Ma=0.2 and Ma=0.4.

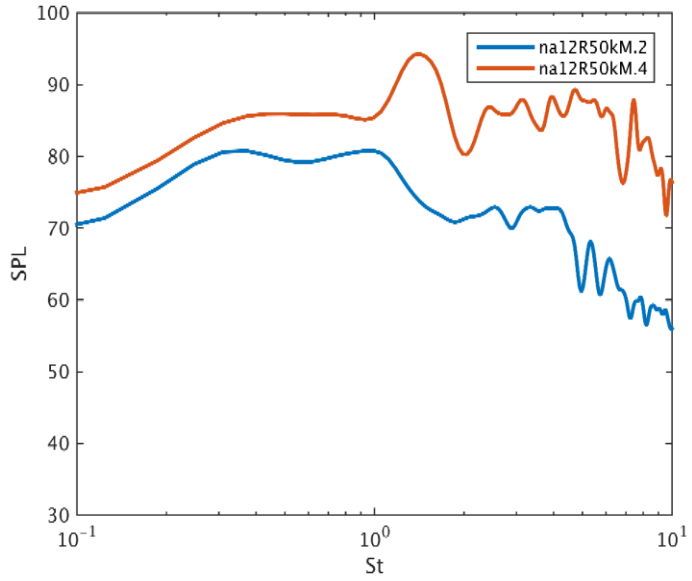

Figure 4.27 SPL vs St for NACA0012 at AOA= 12°, Re=50,000, Ma=0.2 and Ma=0.4.

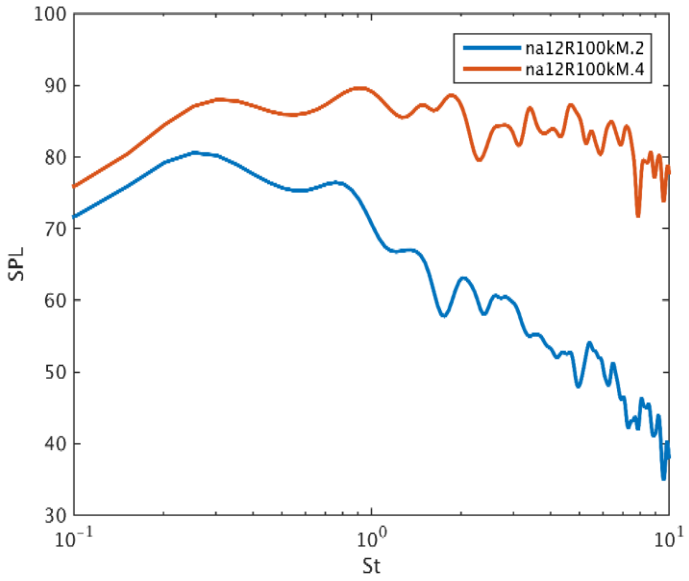

Figure 4.28 SPL vs St for NACA0012 at AOA= 12°, Re=100,000, Ma=0.2 and Ma=0.4.

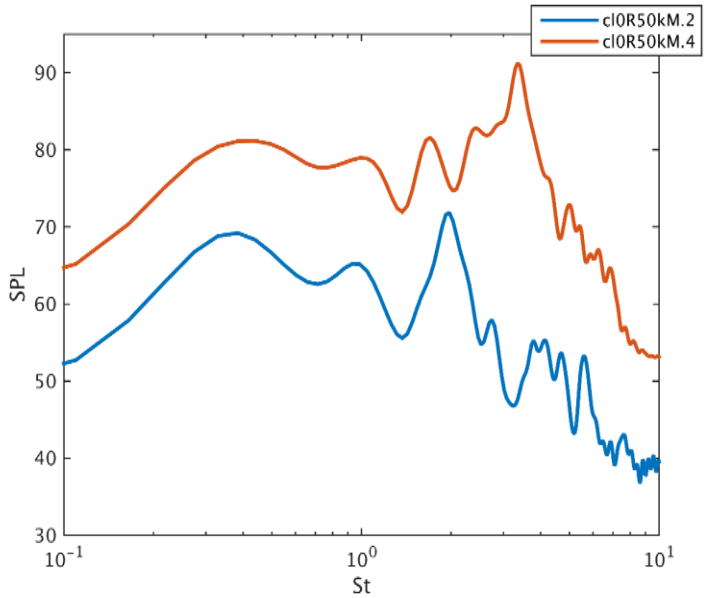

Figure 4.29 SPL vs St for CLARKY at AOA= 0°, Re=50,000, Ma=0.2 and Ma=0.4.

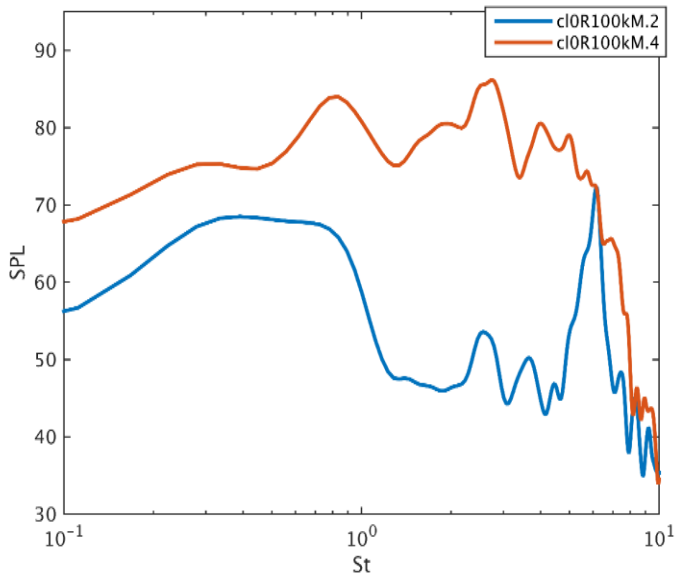

Figure 4.30 SPL vs St for CLARKY at AOA= 0°, Re=100,000, Ma=0.2 and Ma=0.4.

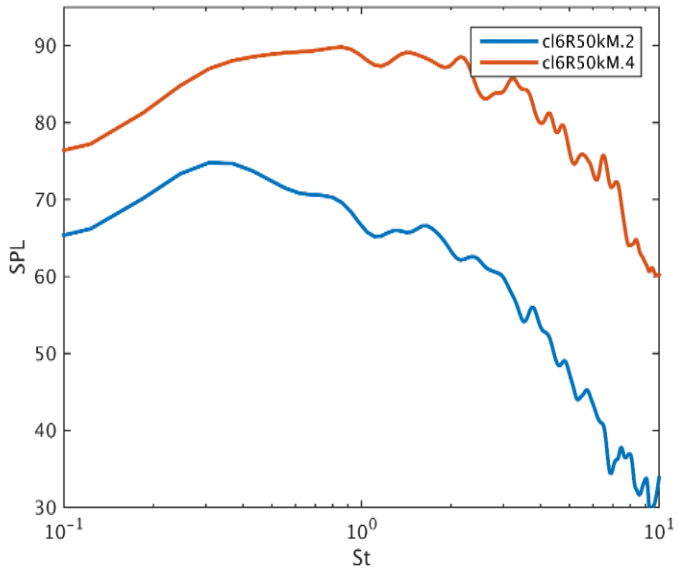

Figure 4.31 SPL vs St for CLARKY at AOA= 6°, Re=50,000, Ma=0.2 and Ma=0.4.

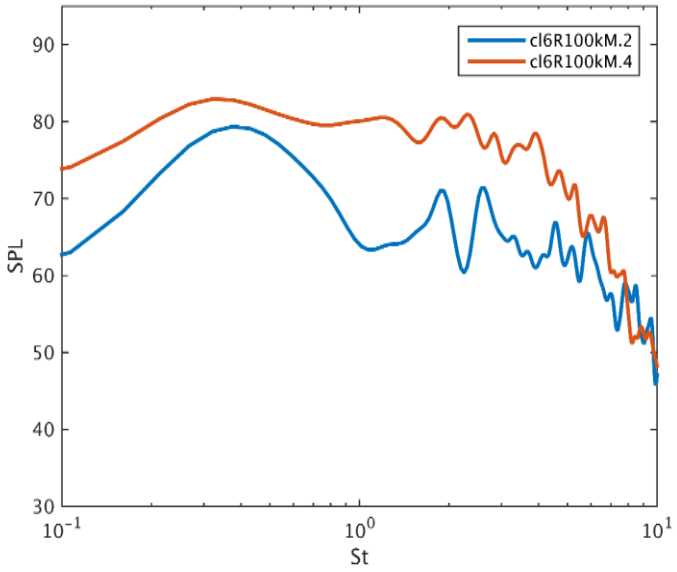

Figure 4.32 SPL vs St for CLARKY at AOA= 6°, Re=100,000, Ma=0.2 and Ma=0.4.

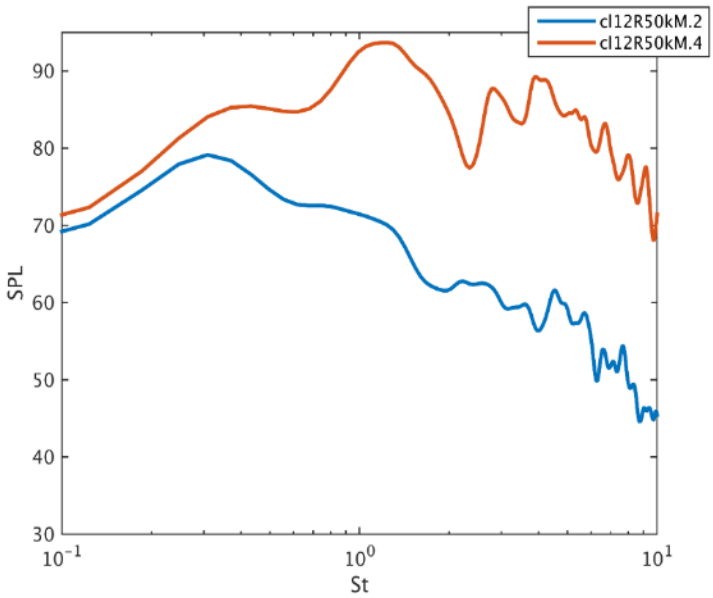

Figure 4.33 SPL vs St for CLARKY at AOA= 12°, Re=50,000, Ma=0.2 and Ma=0.4.

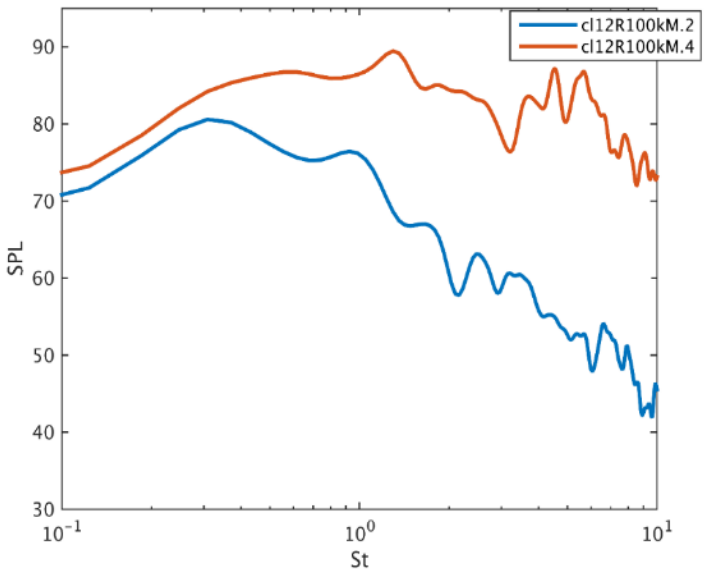

Figure 4.34 SPL vs St for CLARKY at AOA= 12°, Re=100,000, Ma=0.2 and Ma=0.4.

The following figures represent the sound pressure level spectra (SPL) versus the Strouhal number (St) of both NACA 0012 and CLARKY for the same Mach number and at the same Angle of Attack for different Reynolds numbers. Reynolds number does not seem to have a large effect on the SPL at low frequencies, which is expected since the nondimensional distance from the probe location is the same for both cases (so as the Reynolds number is increased, this distance is also increased; since the Mach number and viscosity are the same, the Reynolds number is varied by varying the chord of the airfoil). There are some differences in the SPL at high frequencies.

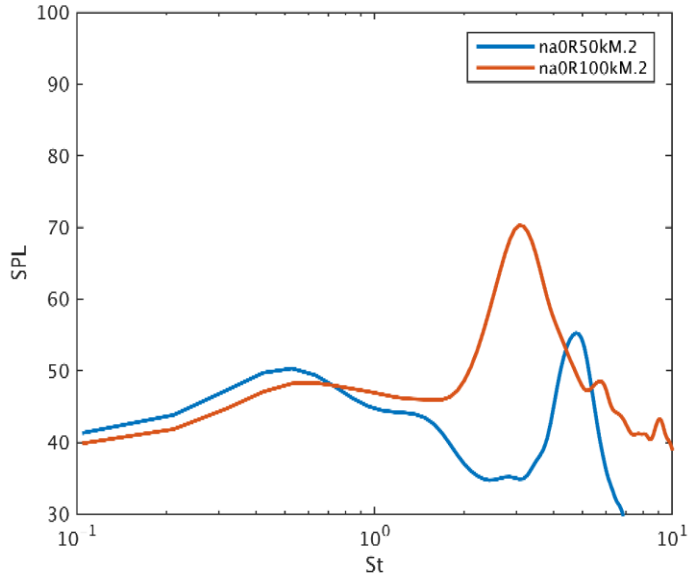

Figure 4.35 SPL vs St for NACA 0012 at AOA= 0°, Ma=0.2, Re=50,000 and Re=100,000.

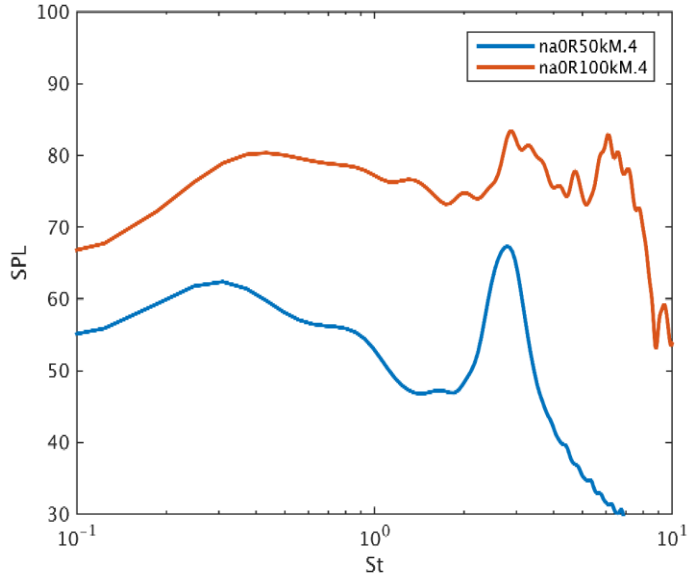

Figure 4.36 SPL vs St for NACA 0012 at AOA= 0°, Ma=0.4, Re=50,000 and Re=100,000.

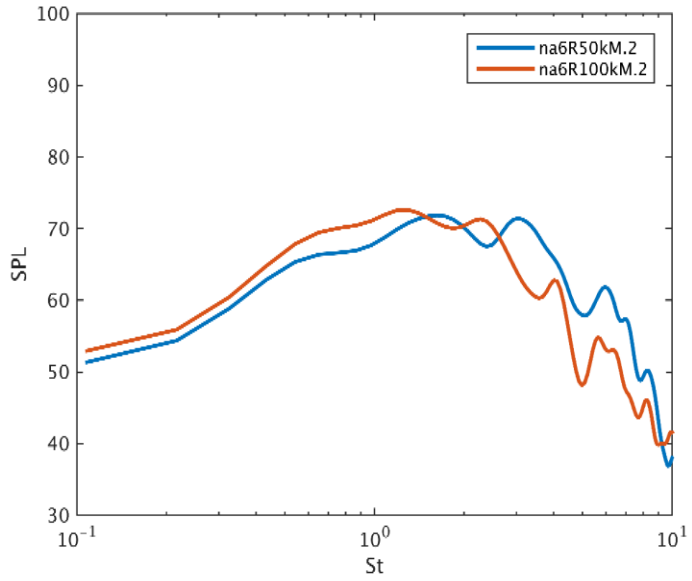

Figure 4.37 SPL vs St for NACA 0012 at AOA= 6°, Ma=0.2, Re=50,000 and Re=100,000.

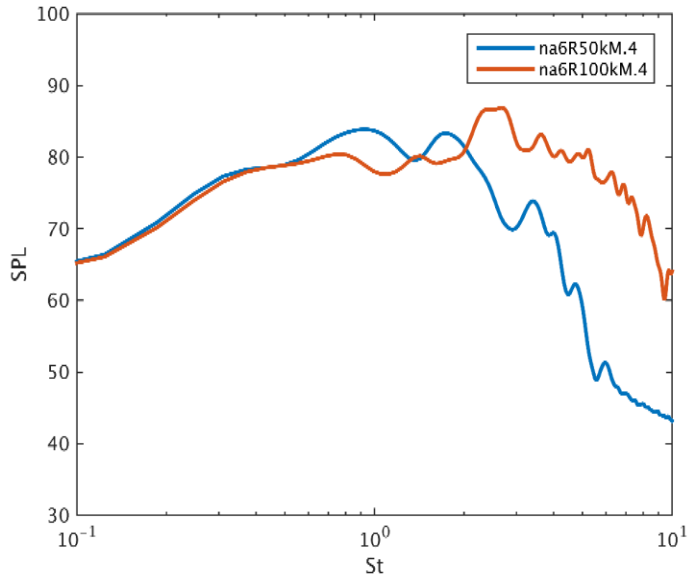

Figure 4.38 SPL vs St for NACA 0012 at AOA= 6°, Ma=0.4, Re=50,000 and Re=100,000.

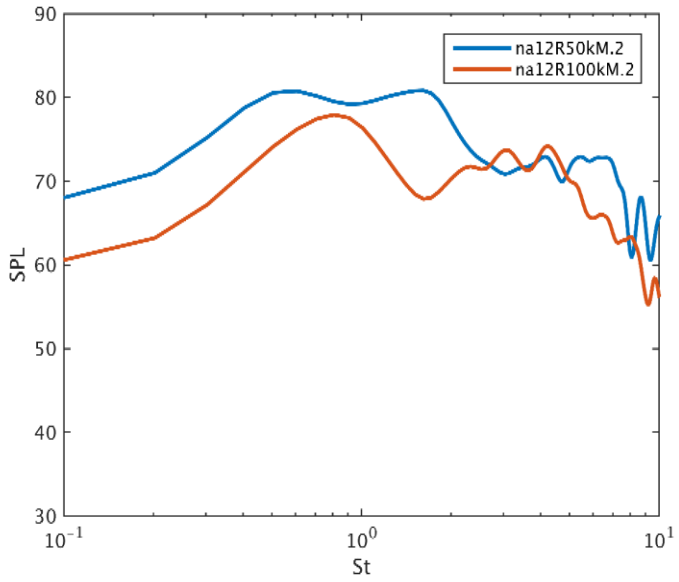

Figure 4.39 SPL vs St for NACA 0012 at AOA= 12°, Ma=0.2, Re=50,000 and Re=100,000.

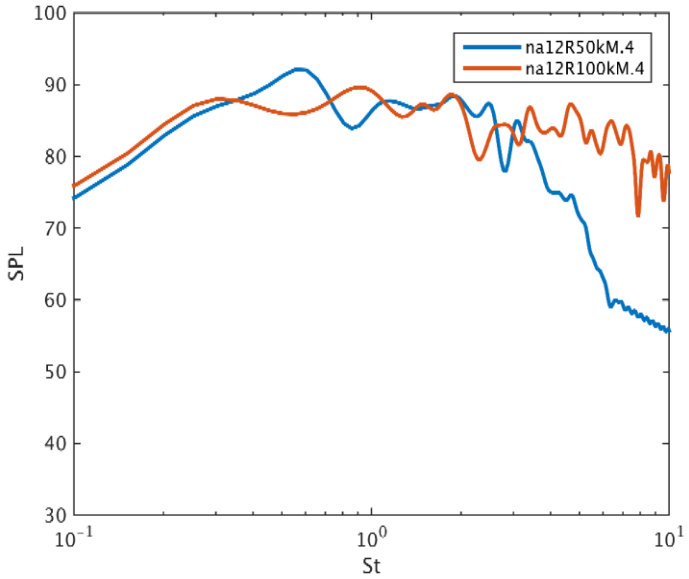

Figure 4.40 SPL vs St for NACA 0012 at AOA= 12°, Ma=0.4, Re=50,000 and Re=100,000.

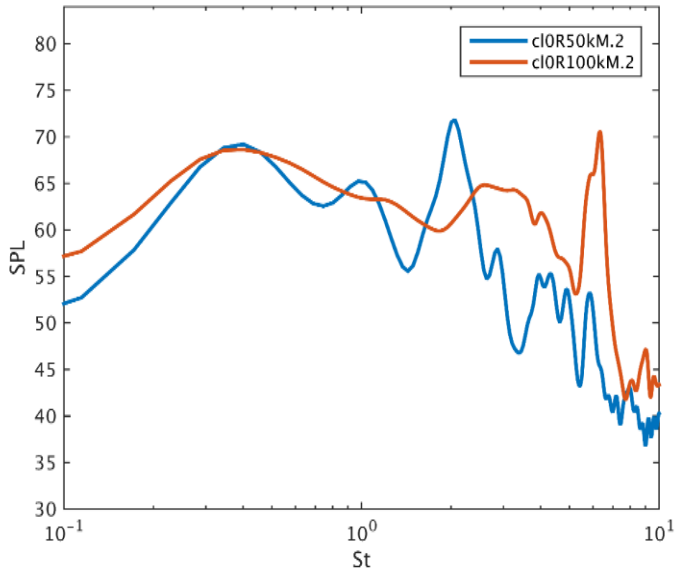

Figure 4.41 SPL vs St for CLARKY at AOA= 0°, Ma=0.2, Re=50,000 and Re=100,000.

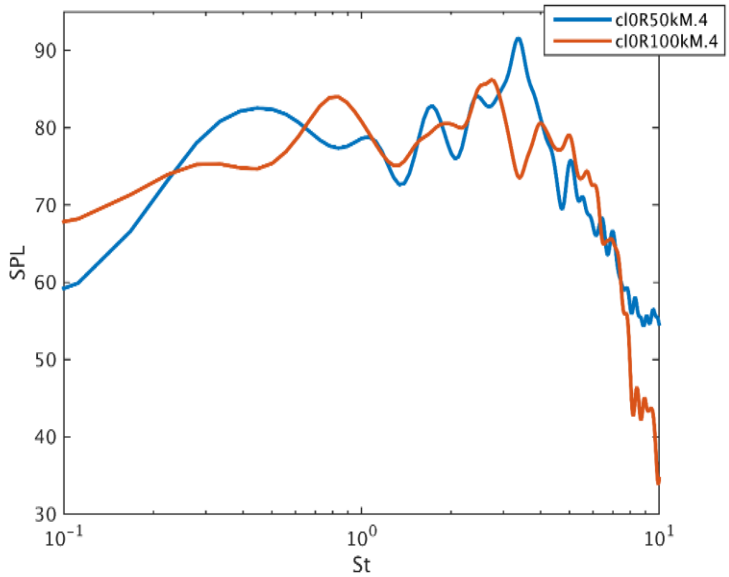

Figure 4.42 SPL vs St for CLARKY at AOA= 0°, Ma=0.4, Re=50,000 and Re=100,000.

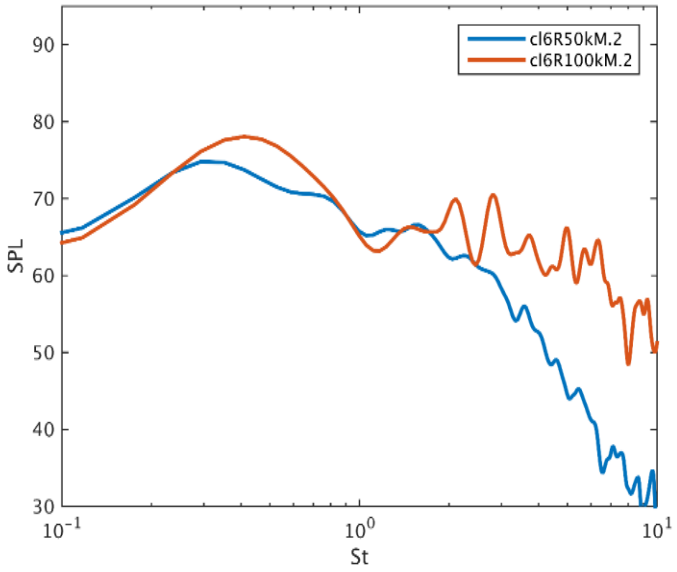

Figure 4.43 SPL vs St for CLARKY at AOA= 6°, Ma=0.2, Re=50,000 and Re=100,000.

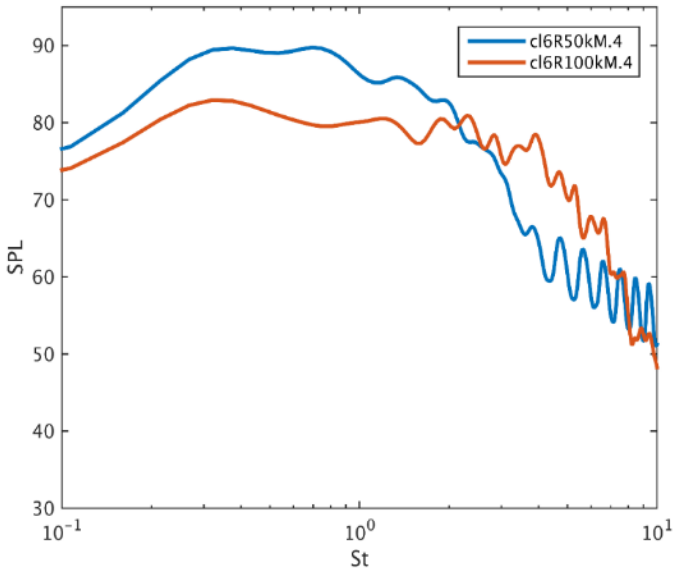

Figure 4.44 SPL vs St for CLARKY at AOA= 6°, Ma=0.4, Re=50,000 and Re=100,000.

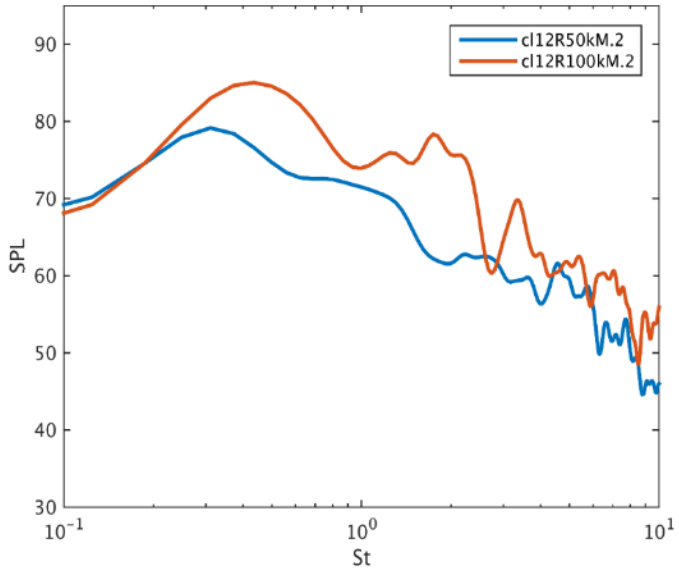

Figure 4.45 SPL vs St for CLARKY at AOA= 12°, Ma=0.2, Re=50,000 and Re=100,000.

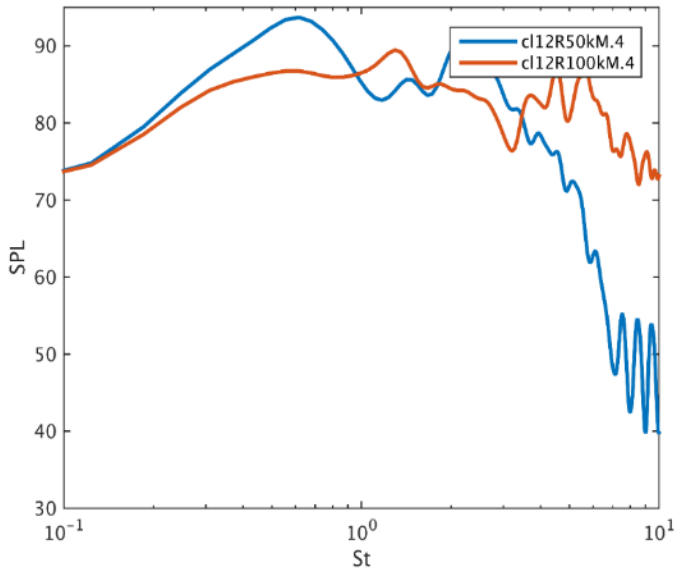

Figure 4.46 SPL vs St for CLARKY at AOA= 12°, Ma=0.4, Re=50,000 and Re=100,000.

Table 4.7 represents the calculations of the Overall Averaged Sound Pressure Level (OASPL) and the peakfrequency for all 24 cases. The Overall Averaged Sound Level Pressure is calculated as follows:

$$OASPL = 10 * log_{10}[dSt * sum(10^{SPL})] \quad (4.2)$$

whereSt represents the Strouhal number and $dSt = dSt2 - dSt1$.

The peak frequency is calculated using the following formula:

$$\text{fp} = \frac{\text{Stp}*\text{Ma}*\text{c}}{\text{chord}} \quad (4.3)$$

where Ma represents the Mach number, c is the speed of sound, and Stp is the Strouhal number associated with the peak SPL. The SPL at r=200 from the source is also included in table 4.7, according to the attenuation formula

$$OASPL2 = OASPL1 - 20 * |log_{10}[r1/r2]| \quad (4.4)$$

Table 4.7 Numerical calculation of the Overall Averaged Sound Pressure Level and the peak Frequency.

Airfoils Type	Angle of Attack	Reynolds number	Mach number	OASPL @ r=8.2	OASPL @ r=200	Peak Frequency
NACA 0012	0°	50000	0.2	71.41	43.66	9520
			0.4	74.49	46.74	19040
		100000	0.2	72.36	44.61	5780
			0.4	85.91	58.16	18380
	6°	50000	0.2	75.07	47.32	7140
			0.4	86.87	59.12	13600
		100000	0.2	76.68	48.93	5100
			0.4	88.23	60.48	16320
	12°	50000	0.2	82.12	54.37	3740
			0.4	94.86	67.11	8160
		100000	0.2	82.79	55.04	3740
			0.4	93.43	65.68	6664
CLARKY	0°	50000	0.2	70.02	42.27	8160
			0.4	88.33	60.58	40200
		100000	0.2	78.67	50.92	23120
			0.4	86.36	58.61	39440
	6°	50000	0.2	76.40	48.65	2380
			0.4	92.08	64.33	15830
		100000	0.2	78.49	50.74	2720
			0.4	85.03	57.28	11560
	12°	50000	0.2	80.49	52.74	1700
			0.4	94.25	66.50	11830
		100000	0.2	81.61	53.86	1360
			0.4	91.79	64.04	10200

For both airfoils (NACA 0012 and CLARKY), the SPL increases as the Mach number and Reynolds number increases (the increase as a function of Re is small). However, at 12° angle of attack, Re=100,000 and Ma=0.4 the SPL decreases slightly when we increase the Reynolds number since in a result of that the chord becomes larger which leads to decrease the noise slightly.

CHAPTER V

CONCLUSION

The characteristics of the aerodynamic noise radiating from an airfoil at various angles of attack, Reynolds numbers and Mach numbers was investigated. The problem was solved using a high-order compressible Navier-Stokes code, with Runge-Kutta explicit time integration and dispersion-relation-preserving spatial discretization. Various results in terms of velocity and pressure distribution around the airfoil, and sound pressure level spectra calculated from different probe points located in the near- and far-field were compared to each other and discussed.

The simulation results- pressure contours, sound pressure level spectra- obtained in this study lead to the following conclusions:

- Contour plots of pressure showedthatincreasing the angle of attack, Reynolds number, and Mach numberseperates the flow leading to generatingvorticesthatcreatesacousticwaves.
- Largervortices and more turbulence intensitywereobsorved for a non-zero angle of attackcamberedairfoilcompared to a symmetricalairfoil.
- SPL spectrashowedthat as weincreaseboth the angle of attackand the Reynolds numberthe noise levelincreases as the Strouhalnumberdecreases.
- Enlarging the chord leads to a slightdecrease in the noise level.

- The peakfrequencyisdecreased as the angle of attack, Reynolds number, and Mach number are increased.
- Overall the noise fromsmallairfoilboundary layer islow in the near-field and verylow in the farfield

Future workwillinclude full three-dimensional simulations, capturing the turbulent boundary layer and the flow separation in three-dimensions. The application of an acousticanalogy to betterpredict the sound radiation to the farfieldisalso a subject of a future study.

REFERENCES

[1] Schlinker, Robert H.: and Amiet, Roy K.: Helicopter Rotor Trialing Edga Noise. NASA CR-3470, 1981. (see also AIAA Paper 81-2001).

[2] Brooks, Thomas F. : and Schlinker, Robert H. : Progress in Rotor Broadband Noise Research. Vertica, vol. 7, no. 4, 1983, pp. 287-307.

[3] Air Traffic Forecasts for the UK 2000, Department of the Environment, Transport and the Regions, 2000.

[4] Guidance to the Civil Aviation Authority on environmental objectives relating to the exercise of its air navigation functions, Department for Transport 2002

[5] This is related to noise above a threshold for 'community annoyance' adopted by the government. This threshold is 57dB(A) Leq and is discussed further in the full report.

[8] Bruce, Kim B. and John Mitchell. PER models of subtyping, recursive types and higher-order polymorphism. In ACM Symposium on Principles of Programming Languages (POPL), Albuquerque, New Mexico, January 1992.

[9] Bechara, W., Bailly, C., Lafon, P., Candel, S. 1994 Stochastic approach to noise modeling for free turbulent flows. AIAA J. 32, 455-463.

[10] Ffowcs Williams, J.E. and Hall, L.H. "Aerodynamic Sound Generation by Turbulent Flow in the Vicinity of a Scattering Half Plane", Journal of Fluid Mechanics, 40, pp 657-670 (1970)

[11] Wang, M. and Moin, P. "Computation of Trailing-Edge Flow and Noise Using Large-Eddy Simulation", AIAA Journal, 38, (12), pp 2201-2209 (2000)

[12] Manhoa, E. Troff, B. and Sagaut, P. "Trailing Edge Noise Prediction Using Large Eddy Simulation and Acoustic Analogy", AIAA Journal, 38, (4), pp 575-583 (2000)

[13] Marsden, A.L., Wang, M., Dennis, J.E. and Moin, D.J.E. "Trailing-Edge Noise Reduction using Derivative-Free Optimization and Large-Eddy Simulation", Journal of Fluid Mechanics, 572, pp 143-159 (2007)

[14] Curle, N. “The Influence of Solid Boundaries on Aerodynamic Sound”, Proceedings of the Royal Society of London, Series A: Mathematical and Physical Sciences, 231, (1187), pp 505-514 (1955)

[15] Ffowcs Willams, J.E. and Hawkings, D.L. “Sound Generated by Turbulence and Surfaces in Arbitrary Motion”, Philosophical Transactions of the Royal Society A, 264, pp 321-342 (1969)

[16] Bechara, W., Bailly, C., Lafon, P. and Candel, S. “Stochastic Approach to Noise Modeling for Free Turbulent Flows”, AIAA Journal, 32, (3), pp 455-463 (1994)

[17] Bailly, C. and Juve, D. “Numerical Solution of Acoustic Propagation Problems Using Linearized Euler Equations”, AIAA Journal, 38, (1), pp 22-29 (2000)

[18] Bogey, C., Bailly, C. and Juve, D. “Computation of Flow Noise Using Source Terms in Linearized Euler Equations”, AIAA Journal, 40, (2), pp 235-243 (2002)

[19] Ewert, R. and Schroder, W. “On the Simulation of Trailing Edge Noise with a Hybrid LES/APE Method”, Journal of Sound and Vibration, 270, pp 509-524 (2004).

[20] Brooks, T., Pope, D. and Marcolini, M. (1989). Airfoil self-noise and prediction. [Washington, D.C.]: National Aeronautics and Space Administration, Office of Management, Scientific and Technical Information Division.

[21] Powell, A. (1959). On the Aerodynamic Noise of a Rigid Flat Plate Moving at Zero Incidence. The Journal of the Acoustical Society of America, 31(12), p.1649.

[22] Williams, J. and Hall, L. (1970). Aerodynamic sound generation by turbulent flow in the vicinity of a scattering half plane. Journal of Fluid Mechanics, 40(04), pp.657-670.

[23] Howe, M. (1978). A review of the theory of trailing edge noise. Journal of Sound and Vibration, 61(3), pp.437-465.

[24] Brooks, T. F.; and Hodgson, T. H.: Trailing Edge Noise Prediction From Measured Surface Pressures. J. Sound 64 Vibration, vol. 78, no. 1, Sept. 8, 1981, pp. 69 117.

[25] Wagner S., Bareiβ R. and Guidati G., “Wind turbine noise,” Springer, 3-540-60592-4, 1996.

[26] Lighthill, M. (1951). On Sound Generated Aerodynamically. I. General Theory. Proceedings of the Royal Society A: Mathematical, Physical and Engineering Sciences, 211(1107), pp.564-587.

[27] Amiet, R. (1976). Noise due to turbulent flow past a trailing edge. Journal of Sound and Vibration, 47(3), pp.387-393.

[28] Chase, D. (1975). Noise Radiated from an Edge in Turbulent Flow. AIAA Journal, 13(8), pp.1041-1047.

[29] Berland, J., Bogey, C. and Bailly, C. (2006), Low-dissipation and low-dispersion fourth-order Runge-Kutta algorithm, Computers and Fluids, Vol. 35, pp. 1459-1463.

[30] Tam, C.K.W. and Webb, J.C. (1993), Dispersion-relation-preserving finite diff erence schemes for Computational Aeroa-coustics, Journal of Computational Physics, Vol. 107, pp. 262-281.

[31] Kennedy, C.A. and Carpenter, M.H. (1997), Comparison of several numerical methods for simulation of compressible shear layers, NASA Technical Report NASA-97-TP3484.

[32] Kim, J.W. and Lee, D.J. (2000) Generalized Characteristic Boundary Conditions for Computational Aeroacoustics, AIAA Journal, Vol. 38, pp. 2040-2049.

APPENDIX A

TIME ACOUSTIC PRESSURE

The following plots represent the time acoustic pressure for different angle of attack, Reynolds number, and Mach number. The noise is calculated in a probe location of coordinates x= 3.53 and y=7.40 chord units, away from the airfoil. Fig A.1 and A.4 shows the pressure fluctuation for a symmetrical airfoil at 0° angle of attack as the Reynolds number and the Mach number are increased. At Re=50,000 and Ma=0.2, the maximum in the pressure fluctuations appears to be 0.18. However, for Re=100,000 and Ma=0.4, the maximum in the pressure fluctuation is increased to 1.5.

For the angle of attack of 6°, the amplitude of pressure fluctuations is higher than the amplitude of pressure fluctuations corresponding to the airfoil at 0° angle of attack. Fig A.15 shows that at Re=50,000 and Ma=0.2, the maximum in the pressure fluctuation is 1.8, and for Re=100,000 and Ma=0.4, the maximum pressure fluctuation is increased to 8.2 as shown in Fig A.7. Fig A.8, A.11 shows the time acoustic pressure for 12° angle of attack, at Re=50,000 and Ma=0.2, the pressure fluctuation appears to be 5.2, and at Re=100,000 and Ma=0.4 the pressure fluctuation is 30.

The cambered airfoil results are shown in Fig A.13, A.14, A.15, A.16, A.17, A.18, A.19, A.20, A.21, A.22, A.23, and A.24. Fig A.13 and A.16 shows the pressure fluctuation for a cambered airfoil at 0° angle of attack as the Reynolds number and the Mach number are increased. At Re=50,000 and Ma=0.2, the pressure fluctuation appears to be 1.4.

However, for Re=100,000 and Ma=0.4, the maximum pressure fluctuation is increased to 4.3. Inclining the angle of attack at 6°, the maximum pressure fluctuation is higher than the airfoil at 0°, Fig A.17 shows that at Re=50,000 and Ma=0.2, the

maximum pressure fluctuation is 3, and for Re=100,000 and Ma=0.4, the maximum pressure fluctuation is increased to 6.1 as shown in Fig A.20.

Fig A.21, A.24 shows the time acoustic pressure for 12° angle of attack, at Re=50,000 and Ma=0.2, the pressure fluctuation appears to be 4, and at Re=100,000 and Ma=0.4 the pressure fluctuation is 14.

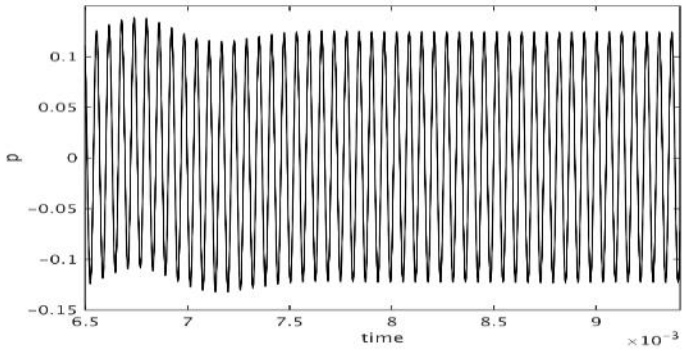

Figure A.1 Time Acoustic Pressure plot for NACA 0012 of AOA=0°, Re=50,000, Ma=0.4.

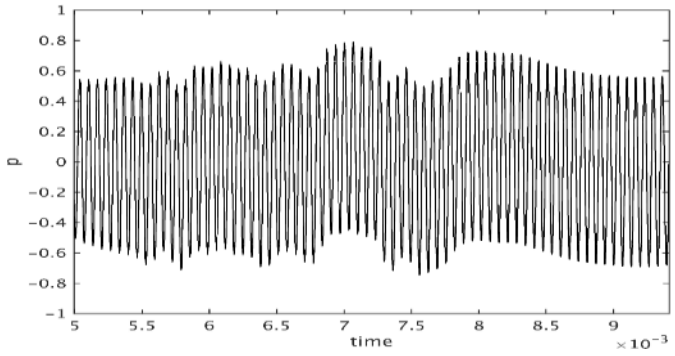

Figure A.2 Time Acoustic Pressure plot for NACA 0012 of AOA=0°, Re=50,000, Ma=0.4.

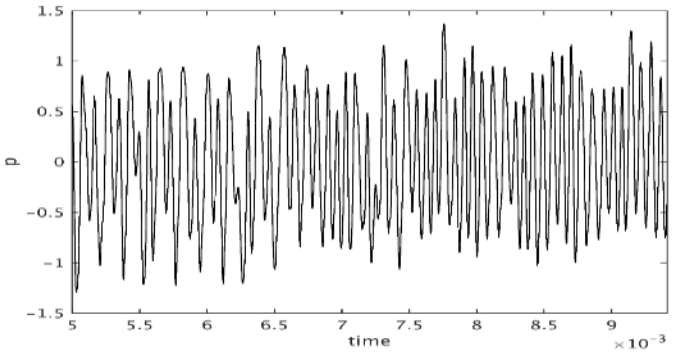

Figure A.3 Time Acoustic Pressure plot for NACA 0012 of AOA=0°, Re=100,000, Ma=0.2.

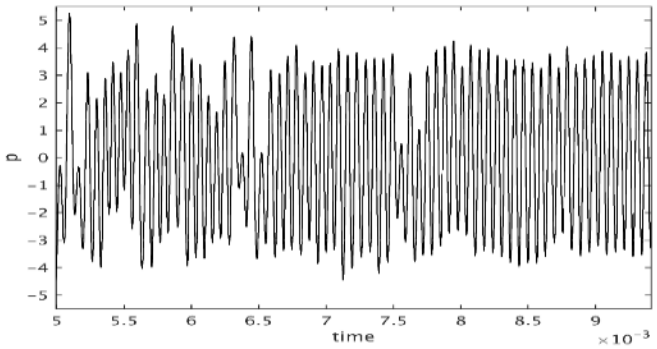

Figure A.4 Time Acoustic Pressure plot for NACA 0012 of AOA=0°, Re=100,000, Ma=0.4.

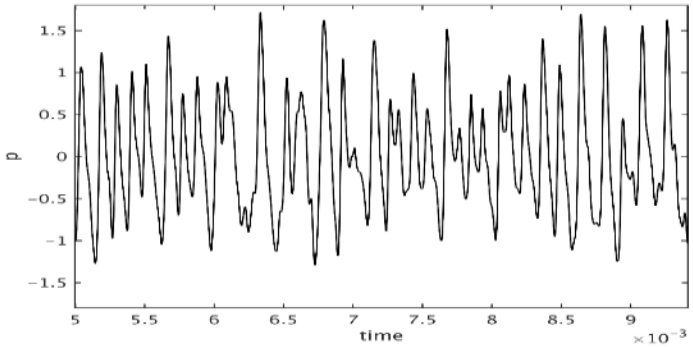

Figure A.5 Time Acoustic Pressure plot for NACA 0012 of AOA=6°, Re=50,000, Ma=0.2.

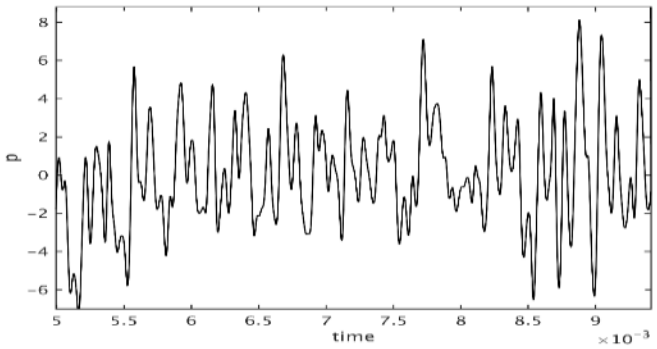

Figure A.6 Time Acoustic Pressure plot for NACA 0012 of AOA=6°, Re=50,000, Ma=0.4.

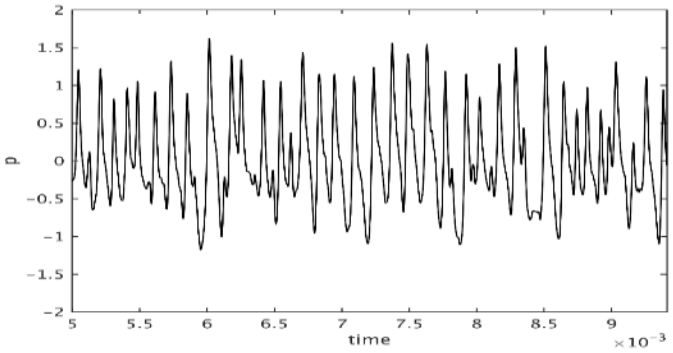

Figure A.7 Time Acoustic Pressure plot for NACA 0012 of AOA=6°, Re=100,000, Ma=0.2.

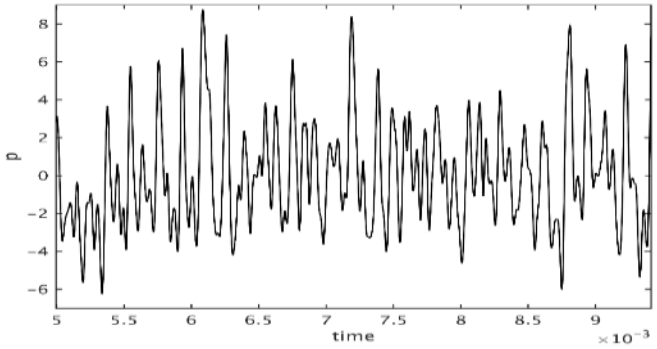

Figure A.8 Time Acoustic Pressure plot for NACA 0012 of AOA=6°, Re=100,000, Ma=0.4.

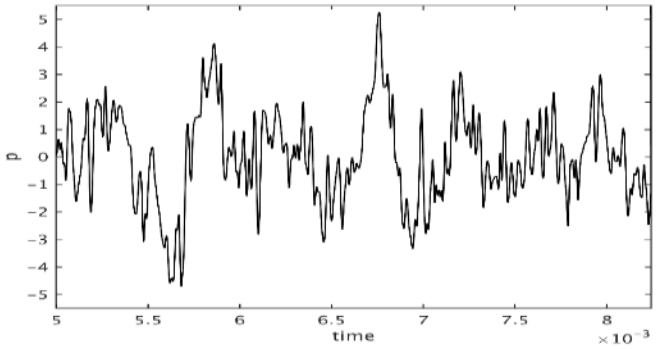

Figure A.9 Time Acoustic Pressure plot for NACA 0012 of AOA=12°, Re=50,000, Ma=0.2.

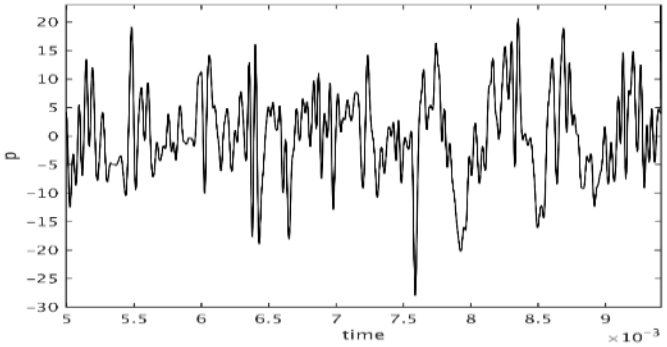

Figure A.10 Time Acoustic Pressure plot for NACA 0012 of AOA=12°, Re=50,000, Ma=0.4.

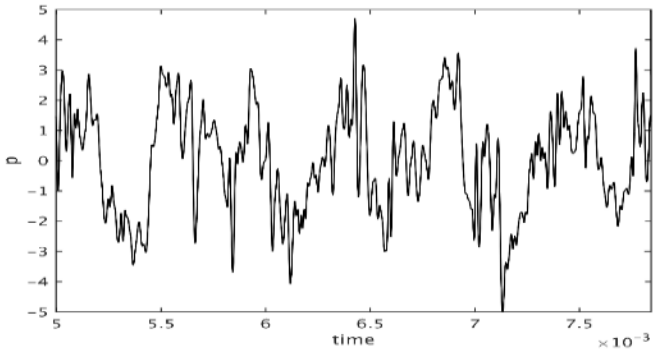

Figure A.11 Time Acoustic Pressure plot for NACA 0012 of AOA=12°, Re=100,000, Ma=0.2.

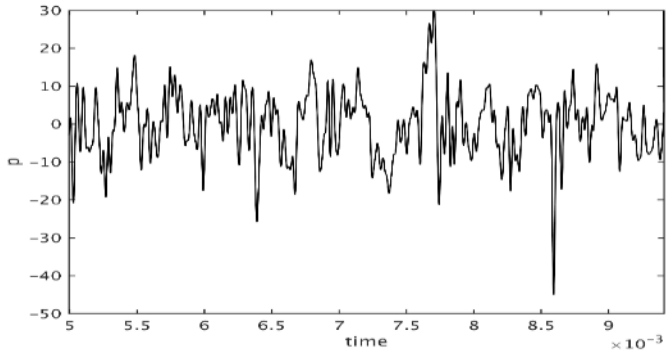

Figure A.12 Time Acoustic Pressure plot for NACA 0012 of AOA=12°, Re=100,000, Ma=0.4.

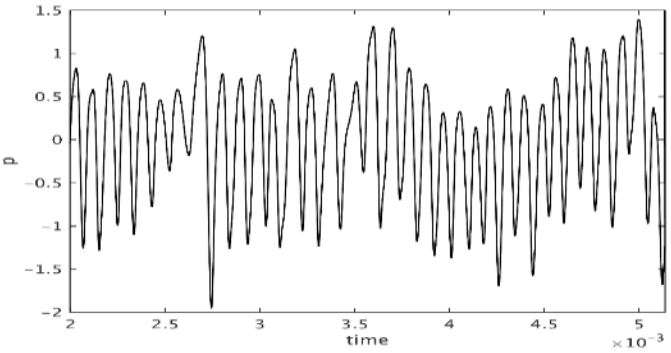

Figure A.13 Time Acoustic Pressure plot for CLARKY of AOA=0°, Re=50,000, Ma=0.2.

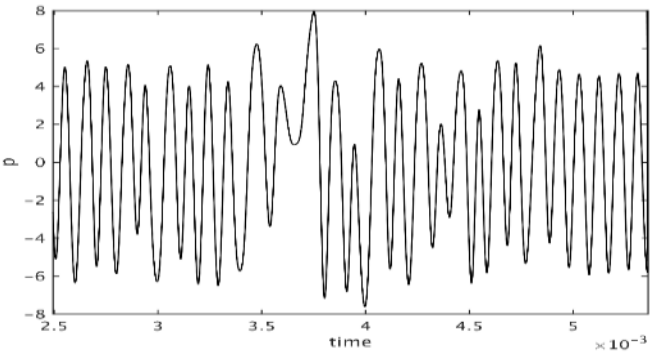

Figure A.14 Time Acoustic Pressure plot for CLARKY of AOA=0°, Re=50,000, Ma=0.4.

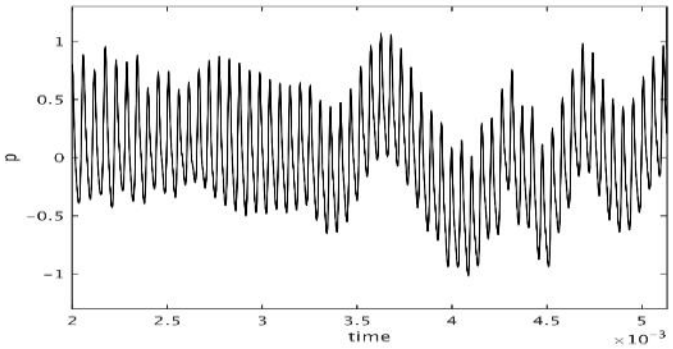

Figure A.15 Time Acoustic Pressure plot for CLARKY of AOA=0°, Re=100,000, Ma=0.2.

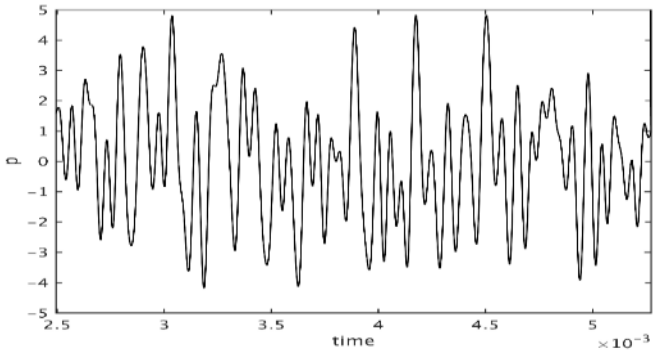

Figure A.16 Time Acoustic Pressure plot for CLARKY of AOA=0°, Re=100,000, Ma=0.4.

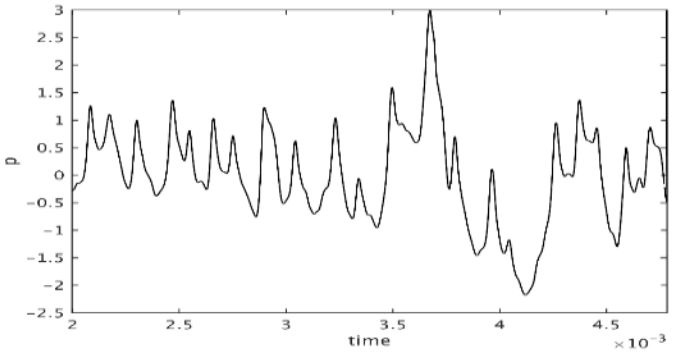

Figure A.17 Time Acoustic Pressure plot for CLARKY of AOA=6°, Re=50,000, Ma=0.2.

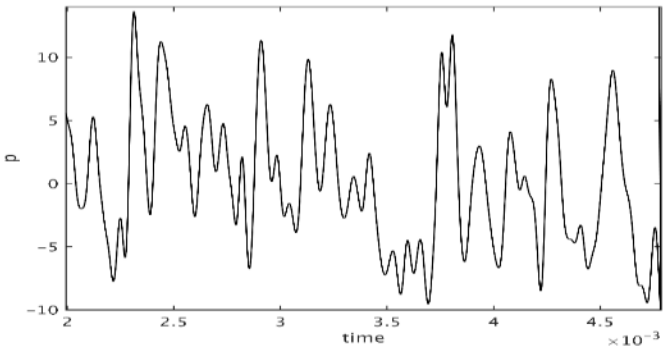

Figure A.18 Time Acoustic Pressure plot for CLARKY of AOA=6°, Re=50,000, Ma=0.4.

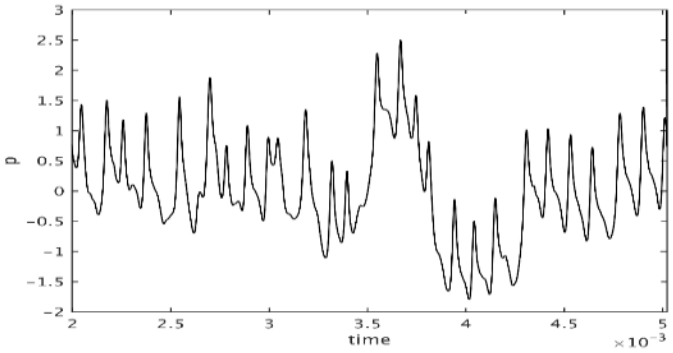

Figure A.19 Time Acoustic Pressure plot for CLARKY of AOA=6°, Re=100,000, Ma=0.2.

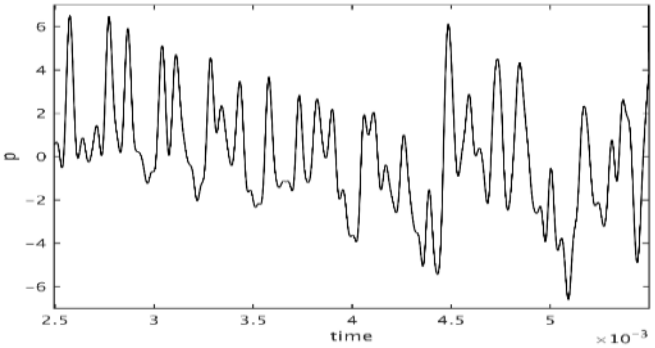

Figure A.20 Time Acoustic Pressure plot for CLARKY of AOA=6°, Re=100,000, Ma=0.4.

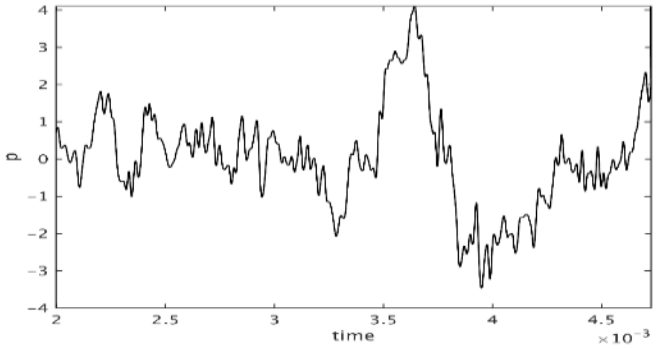

Figure A.21 Time Acoustic Pressure plot for CLARKY of AOA=12°, Re=50,000, Ma=0.2.

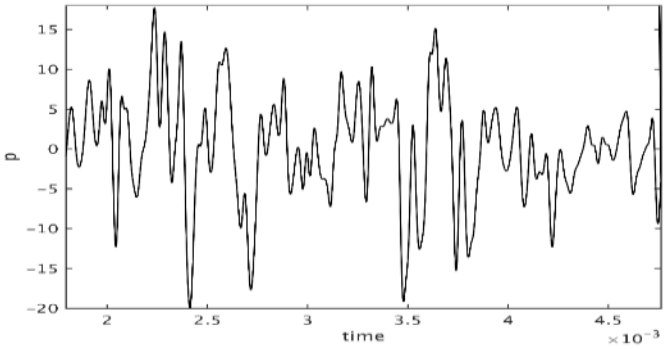

Figure A.22 Time Acoustic Pressure plot for CLARKY of AOA=12°, Re=50,000, Ma=0.4.

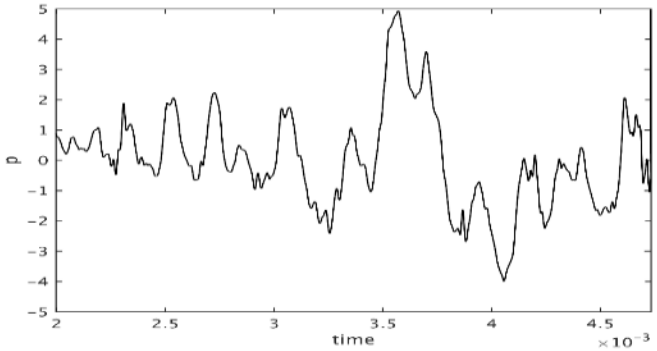

Figure A.23 Time Acoustic Pressure plot for CLARKY of AOA=12°, Re=100,000, Ma=0.2.

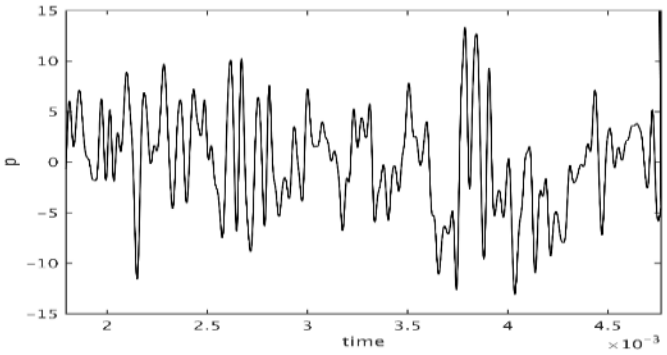

Figure A.24 Time Acoustic Pressure plot for CLARKY of AOA=12°, Re=100,000, Ma=0.4.